# Ingredients of the planet-formation puzzle: Gas substructures and kinematics in transition discs

Wölfer, L.B.

Once I get on a puzzle, I can't get off.

*Richard P. Feynman*

# Chapter 5

# Spirals and meridional flows in the planet-forming disc around HD 100546.

## A multi-line study of its gas kinematics

L. Wölfer, A. F. Izquierdo, A. Booth, S. Facchini,
E. F. van Dishoeck, T. Paneque-Carreño, B. Dent

submitted to A&A

## ABSTRACT

**Context.** The disc around the Herbig star HD 100546 represents a particularly interesting target to study dynamical planet–disc interactions as various features have been observed in both the dust and gas, that provide direct and indirect evidence for ongoing planet formation.

**Aims.** In this work, we aim to analyse the gas kinematics of five molecular CO emission lines ($^{12}$CO 7-6, $^{12}$CO 3-2, $^{12}$CO 2-1, $^{13}$CO 2-1, C$^{18}$O 2-1), observed with ALMA in HD 100546, to reveal deviations from Keplerian rotation as well as substructures in the peak intensity and line width.

**Methods.** For our analysis, we fit the molecular intensity channels with the DISCMINER package to model the line profiles, and extract observables such as centroid velocity, peak intensity, and line width. Aside from fitting the full cube, we also conduct runs where the blue- and redshifted sides are modelled separately to search for possible asymmetries.

**Results.** Our analysis reveals prominent kinematical spiral features in all five lines on large scales of the disc and we reproduce their morphology with both a linear and logarithmic spiral. In $^{12}$CO 2-1, spirals are also seen in the peak intensity residuals, the line width residuals exhibit a prominent ring of enhanced line widths around $125 - 330$ au. The models further show that the emission from the redshifted side originates from higher disc layers than that from the blueshifted side, with the asymmetry being especially pronounced for $^{12}$CO 7-6 and $^{12}$CO 3-2.

**Conclusions.** The pitch angles of the spirals are consistent with those driven by an embedded companion inside of 50 au and they suggest a dynamical mechanism rather than gravitational instabilities. They decrease closer to the midplane, which matches the predictions of Juhász & Rosotti (2018). We further find indications of a companion around 90–150 au, where tentative dips are present in the radial profiles of the integrated intensity of $^{13}$CO and C$^{18}$O 2-1 and pressure minima are observed in the azimuthal velocities. For the first time, we also detect meridional flows in this region, which coincide with the dust gap found by Fedele et al. (2021). The asymmetry in the emission heights may be a result of infall from the disc's environment. Another explanation is provided by a warped inner disc, casting a shadow onto one side of the disc.

## 5.1 Introduction

In order to understand planet formation and the diversity of developed planetary systems such as our own, it is crucial to study the early stages when (proto-) planets are still embedded in their birthplaces – the so-called protoplanetary or planet-forming discs. These discs are not static objects but they evolve and eventually disperse over time with the evolutionary processes not only shaping the disc's appearance but also influencing (and putting a limit on) the planet-formation mechanisms. Conversely, planets interact with their environment, impact disc evolution, and are expected to alter their host disc's structure, for example in terms of density, temperature, or velocity. Even though such young embedded planets may be hidden from the direct eye of our telescopes, their planet–disc interactions still leave observable marks depending on the planet's mass and location.

In the last decade, high-angular-resolution observations of the dust and gas in protoplanetary discs with the Atacama Large Millimeter/submillimeter Array (ALMA; ALMA Partnership et al. 2015), the Spectro-Polarimetric High-contrast Exoplanet REsearch (SPHERE; Beuzit et al. 2019), or the Gemini Planet Imager (GPI; Macintosh et al. 2014) have enabled scientists to search for such signposts of planet–disc interactions. The observations revealed a variety of substructures such as gaps or even cavities, rings, spiral arms, and azimuthal asymmetries to be ubiquitous in both the dust and the gas component (e.g., Bae et al. 2022; Benisty et al. 2022). To interpret the origin of these substructures, it is necessary to understand how frequent they are, to discern possible patterns they follow, and to search for differences or similarities between different star-disc system morphologies.

While various mechanisms such as photoevaporation (e.g., Owen et al. 2011; Picogna et al. 2019), gravitational instabilities (e.g., Kratter & Lodato 2016), magnetorotational instabilities (e.g., Flock et al. 2015, 2017; Riols & Lesur 2019), zonal flows (e.g., Uribe et al. 2015) or compositional baroclinic instabilities (e.g., Klahr & Bodenheimer 2004) have been invoked to explain the observations, at least some of the substructures are expected to be linked to the presence of (massive) planets (Lin & Papaloizou 1979; Zhang et al. 2018). In this context, the so-called transition discs represent a particularly interesting subgroup of young stellar objects (YSOs). These discs are marked by inner regions depleted in dust (and gas) (e.g., Espaillat et al. 2014; Ercolano & Pascucci 2017) and were originally identified through a lack of infrared (IR) excess in their spectral energy distribution (SED; Strom et al. 1989). While they may represent an intermediate (transitioning) state between an optically thick (full) disc and disc dispersal, dynamical clearing by a massive companion represents an alternative explanation: at least some of the cavities – and especially the very deep ones ( e.g., van der Marel et al. 2016) – are expected to be the result of such processes rather than representing an evolutionary state. Transition discs, therefore, represent ideal laboratories to probe disc evolution as well as planet formation models and may enable us to catch planet formation in action.

Ultimately, only a direct detection can confirm the link between the observed disc substructures and an embedded planet. However, the dense and opaque environment of these young planets makes such a task difficult and feasible only for

the very massive, bright planets that are less affected by dust extinction (Sanchis et al. 2020). To date, the only robust detections of forming planets (of several $M_J$) and their circumplanetary discs have been obtained for the PDS 70 system (Keppler et al. 2018; Haffert et al. 2019; Benisty et al. 2021).

The challenge of direct detections and our growing understanding of how planets interact with their host disc have triggered the development of other, indirect, detection techniques. One promising method is to study the velocity field of the rotating gas, observed through molecular line emission, to search for deviations from Keplerian rotation (Pinte et al. 2022). Identifying such variations in the kinematics can be used to probe the local pressure gradient and to characterize the shape of the perturbation. Indeed, several ALMA observations in recent years have reported both localized and extended kinematical deviations, which may be linked to the presence of planets: so-called kink-features are detected by Pinte et al. (2018b, 2019) in HD 163296 and HD 97048 and a Doppler flip is reported in the HD 100546 disc by Casassus & Pérez (2019). Teague et al. (2018a) and Teague et al. (2019a) study the rotation profile of HD 163296, finding perturbations and significant meridional flows that point towards embedded planets. Izquierdo et al. (2022) apply the DISCMINER tool (Izquierdo et al. 2021) – a new channel-map-fitting package able to model the upper and lower disc surfaces simultaneously and to identify localized velocity perturbations in both radius and azimuth – to the same disc and find strong indications for two embedded planets. Extended spiral structures are observed in the kinematical residuals of TW Hya (Teague et al. 2019b, 2022a), HD 100453 (Rosotti et al. 2020a), HD 135344B (Casassus et al. 2021), CQ Tau (Wölfer et al. 2021), HD 163296 and MWC 480 (Teague et al. 2021), and J1604 (Stadler et al. 2023). Non-Keplerian gas spirals are also found in HD 142527 by Garg et al. (2021).

Aside from the kinematics, it is also interesting to study the patterns in the peak intensity/brightness temperature as well as line widths, which are both shaped by the presence of companions and can be used to trace density substructures, vertical motions, or also turbulence. Planets can create density waves that result in an increased surface density and thus higher opacity, moving the $\tau = 1$ layer to a higher altitude where the temperature is generally higher (Phuong et al. 2020a,b). This leads to spiral substructures in the gas brightness temperature. Thermal spiral features are reported in TW Hya by Teague et al. (2019b) and in CQ Tau by Wölfer et al. (2021). These observations may be explained by the models of Muley et al. (2021), who investigate the temperature structure in planet-driven spiral arms. Wölfer et al. (2023) study the gas brightness temperature (and kinematics) of a sample of 36 transition discs, finding significant substructures such as spirals in eight sources. Around the orbit of a massive planet, turbulent motions are triggered which are expected to result in enhanced line widths. Izquierdo et al. (2022) indeed observe an enhancement of line widths around the gas gap at 88 au in HD 163296, which further supports their findings of a planet candidate at 94 au. Enhanced line widths are also found in HD 135344B by Casassus et al. (2021).

In this work, we present a multi-line study of CO gas emission in the transitional disc HD 100546, one particularly interesting target to study planet–disc interactions. The young Herbig Be star, located at ∼110 pc from the Earth (Gaia

Collaboration et al. 2018), is surrounded by a massive disc spanning several hundreds of au and showing various indications of ongoing planet formation, as described in the next section. For our analysis, we apply the DISCMINER package presented in Izquierdo et al. (2021) to archival B6 ($^{12}$CO 2-1, $^{13}$CO 2-1, C$^{18}$O 2-1), B7 ($^{12}$CO 3-2), and B10 ($^{12}$CO 7-6) data to search for perturbations in the velocities, intensities, and line widths (possibly linked to embedded planets) and to obtain the vertical structure of the disc. Probing different layers of the disc with various isotopologues or transitions of the same molecule (as done in this study) or different molecules (e.g., Paneque-Carreño et al. 2023) is crucial to understand how the observed substructures vary and can help us to access their formation mechanism (e.g., Pinte et al. 2018a; Law et al. 2021b). We describe the source and observations in Sect. 5.2. Our modelling approach is detailed in Sect. 5.3 and the results are presented in Sect. 5.4. The latter are discussed in Sect. 5.5 and summarized in Sect. 5.6.

## 5.2 Observations

### 5.2.1 The HD 100546 system

In Fig. 5.1, we show the possible morphology of the HD 100546 system further described in the following. Observations of a compact source (in $L'$-Band) have been interpreted as direct evidence of an embedded companion in the outer disc at $\sim 53$ au (Quanz et al. 2013, 2015; Currie et al. 2015), also known as the giant planet candidate HD 100546 b. Subsequent $Ks$-Band observations, however, revealed a faint extended emission around the same location (Boccaletti et al. 2013) and thus the planetary origin of the observed feature yet needs to be confirmed. Another giant planet, HD 100546 c, may be located at $\sim$14 au, just inside the dust cavity. First postulated by Acke & van den Ancker (2006) and later identified as a point source in near-infrared scattered light data taken with GPI (Currie et al. 2015), the detection of HD 100546 c has been debated in the literature (e.g., Follette et al. 2017; Currie et al. 2017). The presence of the planet is supported by studies on the time variations of ro-vibrational CO emission lines (Brittain et al. 2009, 2013, 2014, 2019), tracing the inner edge of the disc. These observations showed an excess of CO P(26) line emission between 2003 and 2013 – consistent with an orbiting planet – that disappeared in 2017 as the possible planet moved behind the near side of the inner rim of the outer disc. Assuming a common origin, the feature observed in the scattered light is expected to disappear as well and recent observations with VLT/SPHERE indeed lack a detection (Sissa et al. 2018).

Alongside the direct measurements, the HD 100546 disc also exhibits a number of indirect evidence for planet–disc interactions. The scattered light images are marked by spiral structures (e.g., Garufi et al. 2016; Follette et al. 2017) and the millimetre continuum, well studied with ALMA, reveals a large inner cavity ($\lesssim$ 20 au) with the dust being concentrated into two prominent rings between 20–40 au and 150–250 au (e.g., Walsh et al. 2014; Pineda et al. 2019; Fedele et al. 2021). Models show that these substructures are consistent with two giant planets orbiting at locations of 10–15 au and 70–150 au (Pinilla et al. 2015; Fedele et al.

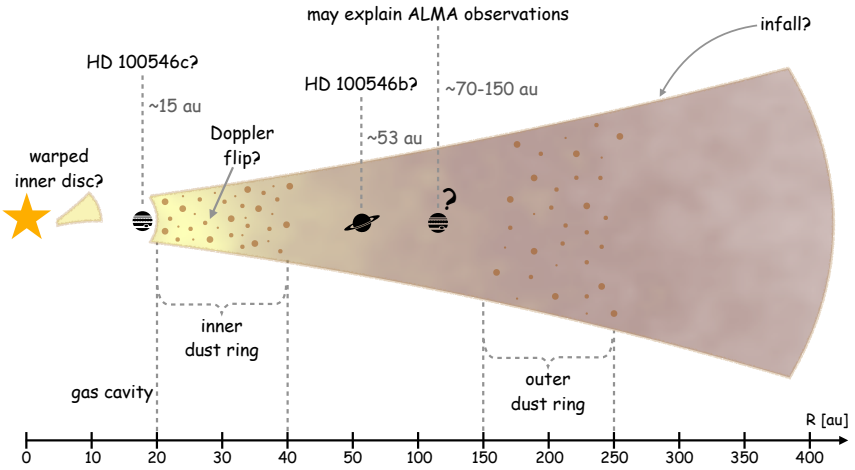


**Figure 5.1:** Possible morphology of the HD 100546 system. Substructures such as the dust rings have been observed, while the planet candidates have been proposed to explain the observations. The two planets suggested in the dust gap may refer to the same object for which the actual location is yet undetermined.

2021; Pyerin et al. 2021). In addition to the dust, the gas disc of HD 100546 has been studied through a range of molecular tracers. ALMA observations of the CO isotopologues are numerous and show that the disc is much more extended in the gas than in the dust (e.g., Walsh et al. 2014; Miley et al. 2019).

The $^{12}$CO emission revealed non-Keplerian features in the kinematics that may be a signpost of ongoing planet formation: Walsh et al. (2017) find asymmetries that could be explained by a warped inner disc, which however stands in contrast to SPHERE observations of the disc by Garufi et al. (2016), who suggest radial flows mediated by planets as an alternative explanation. A warp has also been proposed by Panić et al. (2010) to account for asymmetric line observations ($^{12}$CO $J = 6-5$ and $J = 3-2$) from APEX. As mentioned before, Casassus & Pérez (2019) detect a Doppler flip at ∼28 au which is in agreement with the spiral wake created by a planet and coincides with a fine ridge in the millimetre continuum, suggesting a complex dynamical scenario. The Doppler flip is confirmed by Casassus et al. (2022), with the blueshifted side of the flip however disappearing when vertical and radial flows are taken into account. The authors propose an embedded outflow, launched by a companion of several $M_{\mathrm{Earth}}$, as a possible explanation. This could explain the observations by Booth et al. (2018), who detect non-Keplerian features in the blueshifted side of SO line emission that may be tracing a disk wind, a warped disc, or an accretion shock onto a CPD. Follow-up observations by Booth et al. (2023) support that the azimuthal SO asymmetry is indeed tracing an embedded planet. Another interpretation of the Doppler flip as being the kinematic counterpart of the NIR spiral is proposed by Norfolk et al. (2022). Pérez et al. (2020) analyse the wiggles seen in the velocity channels of $^{12}$CO, $^{13}$CO, and C$^{18}$O. They find that these substructures are in agreement with a massive planet,

with the strength of the wiggles decreasing for $^{13}$CO and C$^{18}$O as expected from planet–disc interaction models. However, as shown by Izquierdo et al. (2021), such kink-like features can also be caused by a gap or density substructures rather than a planet and caution needs to be exercised in the interpretation of these perturbations.

HD 100546 is known to still be embedded in a faint envelope (Grady et al. 2001; Ardila et al. 2007), reaching out to about 1000 au. Such an envelope may be linked to secondary accretion events due to infalling material onto the disc, which is often accompanied by arc-shaped structures as observed in HD 100546 (Dullemond et al. 2019). Asymmetric accretion from an envelope can result in a tilt of the disc (Thies et al. 2011), the formation of vortices (Bae et al. 2015), or drive spirals due to accretion shocks, that propagate the disc (Lesur et al. 2015; Hennebelle et al. 2017). Spirals have been observed in HD 100546 in both the optical (Grady et al. 2001; Ardila et al. 2007) and the near-infrared (Avenhaus et al. 2014; Sissa et al. 2018).

In this paper, we aim to shed some additional light onto the observed kinematical deviations by analysing different CO tracers in data sets that cover both the inner and outer disc with the channel map fitting package DISCMINER.

### 5.2.2 ALMA observations

Molecular line emission of the disc around HD 100546 has been observed with ALMA in several frequency bands. In this paper, we make use of the data sets 2011.0.00863.S (PI: C. Walsh; Walsh et al. 2014), 2015.1.00806.S (PI: J. Pineda; Pineda et al. 2019), 2016.1.00344.S (PI: S. Pérez; Pérez et al. 2020), and 2018.1.00141.S (PI: B. Dent) that cover CO isotopologues in Bands 6, 7, and 10. Their properties are summarized in Table 5.1. For all of the data sets, we started with the archival pipeline-calibrated data and performed further reduction using CASA version 5.7.0 (McMullin et al. 2007).

The Band 6 data of the $^{12}$CO, $^{13}$CO, and C$^{18}$O $J = 2-1$ line were taken in two configurations during Cycle 4, an extended (C40-9) as well as a compact configuration (C40-6) with the same spectral setting. We self-calibrated and combined these data following the same procedure as described in Czekala et al. (2021): we self-calibrated the short-baseline data first and then combined it with the calibrated long-baseline data, after ensuring that the data sets share a common phase centre. Afterwards, we applied further iterations of self-calibration, both in phase and amplitude.

For the combination of the Band 7 data, we took a slightly different approach as the data sets do not share a significant overlap in the spectral settings (aside from both targeting the $^{12}$CO $J = 3 - 2$ line). The long-baseline data taken during Cycle 3 have insufficient short baselines to properly recover spatial scales $> 1\farcs0$. To improve this, we combined the data with observations from Cycle 0. We note, that since these observations were taken in different cycles and taken with different settings, they are not optimal for data combination. Each data set was first self-calibrated (phase and amplitude) individually. The Cycle 0 data were initially pipeline calibrated in CASA version 3.4 and therefore we applied

**Table 5.1:** Observational properties of the ALMA data sets used in this work.

| Project ID | Date | Baselines (m) | Int. time (min) | Central freq. (GHz) | Bandwidth (MHz) | $\Delta v$ ($\mathrm{km\,s^{-1}}$) | Ang. res. ($''$) | LAS ($''$) |
|---|---|---|---|---|---|---|---|---|
| 2011.0.00863.S Cycle 0 | 18 Nov 2012 | 21–375 | 12 | 345.798 | 469 | 0.211 | 0.57 | 6.66 |
| 2015.1.00806.S Cycle 3 | 02 Dec 2015 | 17–10800 | 30 | 345.796 | 469 | 0.212 | 0.035 | 0.471 |
| 2016.1.00344.S Cycle 4 | Oct 2016 - Sep 2017 | 19–12200 | 35, 117 | 230.538<br>220.399<br>219.560 | 117 | 0.158 | 0.183, 0.037 | 1.983, 0.745 |
| 2018.1.00141.S Cycle 6 | 14 Apr 2019 | 15–780 | 28 | 807.499 | 1875 | 0.181 | 0.165 | 2.007 |

the CASA task *statwt* to these data to account for the change in the visibility weight initialization and calibration across different CASA versions $< 4.3$ [1]. The self-calibrated data sets were then combined after ensuring they share a common phase centre. For the Band 10 data, no self-calibration was performed due to a lack of signal-to-noise-ratio (SNR).

The continuum was subtracted using the `uvcontsub` task, flagging channels that contained line emission. We then imaged the lines with `tCLEAN` for both the continuum-subtracted and non-subtracted data sets. In the cleaning process, we used a Briggs robust weighting of +0.5, the 'multi-scale' deconvolver, and a Keplerian mask [2]. A slight `uv-taper` was applied in all Bands in order to improve the SNR in the images. The properties of the final images are summarized in Table 5.2. As high spectral resolution is essential to study kinematics, we imaged the lines with the best possible spectral resolution. However, to ease comparison between the lines, we also made images for the same velocity resolution, given by the lowest resolution among the data sets (B7, $210\,\mathrm{m\,s^{-1}}$). Since the Band 6 and 7 data are a combination of multiple configurations, we applied the JvM correction to the CLEAN images (Jorsater & van Moorsel 1995). This method aims to correct for imaging artefacts induced by the non-gaussianity of the dirty beam. The resulting epsilon values, the ratio of the CLEAN beam volume to the dirty beam volume, are given as 0.56 for Band 6 and 0.22 for Band 7.

In Figs. 5.A.1 and 5.A.2, we show a comparison between the final images of the individual and combined data sets for the Band 7 $^{12}$CO $J = 3 - 2$ line, where it becomes very clear that the inclusion of the shorter baseline data significantly improves the recovery of flux and image fidelity in the outer disk.

**Table 5.2:** Characteristics of the data for the five lines analysed in this work.

| Line | $\Delta v$ ($\mathrm{km\,s^{-1}}$) | Beam ($''$) | RMS ($\mathrm{mJy\,beam^{-1}}$) | Line peak ($\mathrm{mJy\,beam^{-1}}$) |
|---|---|---|---|---|
| $^{12}$CO 2-1 | 0.17 | 0.10x0.08 | 0.6 | 59 |
| $^{13}$CO 2-1 | 0.17 | 0.10x0.08 | 0.6 | 25 |
| C$^{18}$O 2-1 | 0.17 | 0.10x0.08 | 0.5 | 17 |
| $^{12}$CO 3-2 | 0.21 | 0.12x0.09 | 1.7 | 192 |
| $^{12}$CO 7-6 | 0.185 | 0.23x0.17 | 49.9 | 4116 |

### 5.2.3 Observational results

In Fig. 5.2 we present the continuum-subtracted intensity channels of the five CO lines in steps of three from the central channel and for the same channel spacing of $210\,\mathrm{m\,s^{-1}}$. The inner continuum ring is overlaid as dashed contours, showing that the gas disc is much more extended than the dust disc. As seen in the first three rows of Fig. 5.2, the $^{12}$CO data appear elevated with the lower surface of

[1] `https://casadocs.readthedocs.io/en/stable/notebooks/data_weights.html`
[2] `https://github.com/richteague/keplerian_mask`

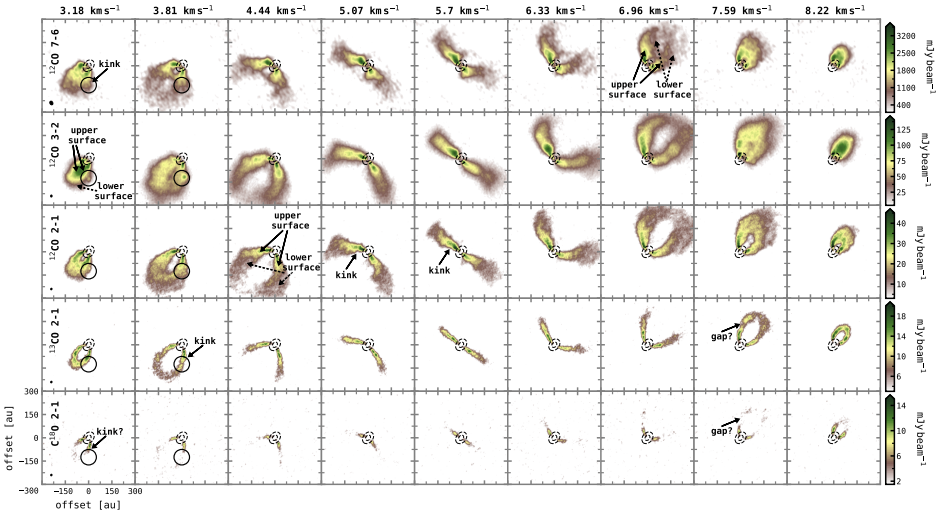


**Figure 5.2:** Examples of the intensity channels of the five CO lines, shown in steps or three from the central channel and for a velocity resolution of 210 m s$^{-1}$. The inner ring of the millimetre continuum is overlaid as dashed contours. A localized feature is seen in some of the channels within the solid circle. The beam of the observation is indicated in the bottom left corner of the first column panels.

the disc being at least partly visible. The other two isotopologues, shown in the bottom two rows, on the other hand, appear rather flat and the lower surface can not be distinguished. This suggests that the emission from these molecules comes, as generally expected (Law et al. 2021b), from lower heights in the disc located closer to the midplane. For these rarer isotopologues, line wing emission may be missing due to sensitivity effects.

In the first two channels of the $^{12}$CO 3-2 data, a bright spot is visible at a separation of $\sim$ 100 au to the south of the central star, highlighted by the solid black circle in Figs. 5.2 and 5.A.1. As those data represent a combination of ALMA Cycle 0 and Cycle 3 data, both time variations and a difference in the observational setups may lead to imaging artefacts. It could further be the result of a projection effect. However, looking at the other lines, a similar, yet much weaker spot is present in the $^{12}$CO 2-1 data and a wiggle or break can be discerned in the corresponding $^{12}$CO 7-6 and $^{13}$CO 2-1 channels around this area. Altogether, this points towards the localized feature being real, but higher sensitivity data including both the long and the short baselines in the same observational setup are needed to support this claim. Continuum subtraction can be ruled out as a cause for the substructure as the continuum ring is located much closer to the star. A comparison of the combined data with the long- and short-baseline data is included in Appendix 5.A.

The channels of $^{12}$CO 7-6 appear to be very asymmetric: the iso-velocity curves seem to be twisted in the centre with the two sides bending in opposite directions. Expected to come from the highest layers of the disc, this may result from interac-

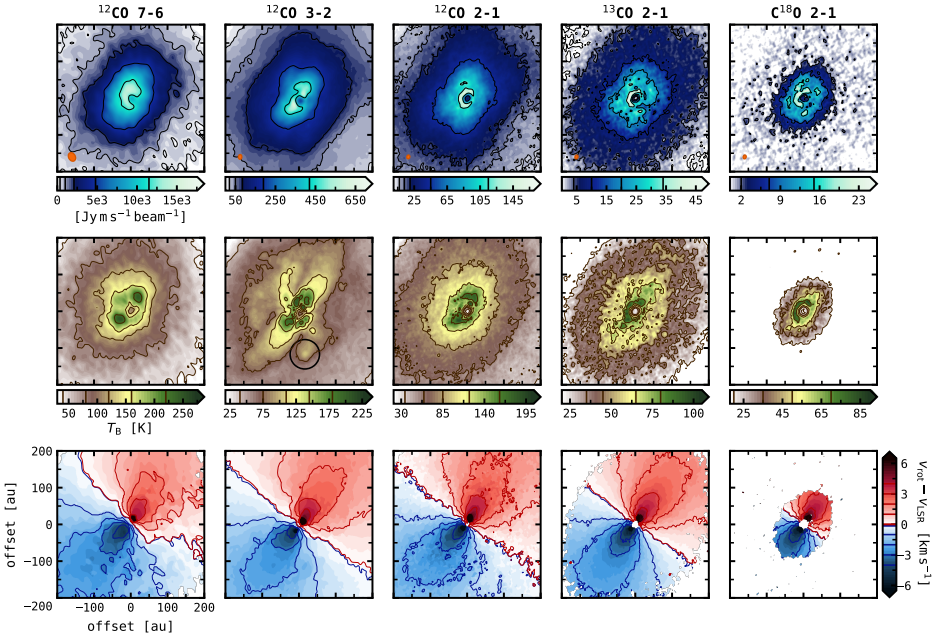


**Figure 5.3:** Integrated intensity (top), peak intensity (middle), and line-of-sight velocity (bottom) of the five CO lines studied here. A localized feature is seen in $^{12}$CO 3-2 around 125 au, marked by the solid circle. Some contours are overlaid and their levels are indicated in the colour bars. The beam of the observation is shown in the bottom left corner of the first-row panels.

tions with material surrounding the disc but could also point towards misaligned disc regions (e.g., Walsh et al. 2017; Facchini et al. 2018). Furthermore, the northeast side of the disc appears to be brighter than the southwest side of the disc.

The $^{13}$CO and C$^{18}$O data show tentative signs of an outer intensity gap in the disc, becoming most prominent for the 7.59 km s$^{-1}$ channel, but higher sensitivity data are needed to confirm its presence. As mentioned in previous work (Pérez et al. 2020), several of the velocity channels are marked by wiggles or kink-like features in their profile, some of which are annotated in Fig. 5.2.

In Fig. 5.3 we show the integrated and peak intensity maps alongside the kinematics for all five lines. These maps were computed with the BETTERMOMENTS package (Teague & Foreman-Mackey 2018) and in case of the peak intensity converted to units of Kelvin with the Planck law. While the intensity maps were obtained with the standard moment 0 and 8 implementations, respectively, the kinematics were derived with the quadratic method. In this approach, a quadratic function is fitted to the brightest pixel in the spectrum as well as the two neighbouring pixels to find the centroid of the line in pixel coordinates. For the peak intensity, we used the non-continuum-subtracted data cube, for the other two quantities the continuum-subtracted data cube. For optically thick lines, continuum subtraction can remove part of the line emission and artificially lower the peak in-

tensity, as part of the underlying continuum is absorbed (e.g., Weaver et al. 2018; Rosotti et al. 2021; Bosman et al. 2021). While we did not apply any masking in the computation of the peak intensity maps, a Keplerian mask was included in the computation of the integrated intensity, and for the kinematics we selected a masking for regions below a certain SNR to reduce the noise at the disc's edge (between 4.5–5).

As seen in the intensity maps, an inner gas cavity ($< 20\,\mathrm{au}$) is present in all isotopologues and lines. At the same location as in the channel maps, a localized, however weak spot is seen in the peak intensity of $^{12}$CO 3-2 (black circle in Figs. 5.3 and 5.A.2), the other lines are lacking a similar feature at this location. In general, the $^{12}$CO 3-2 intensities appear to be very asymmetric, with a cross-like – or possibly spiral-like – structure extending towards the north and south. Again, caution should be exercised with regard to these substructures, as artefacts may have been introduced through the combination of data sets. In Fig. 5.A.2 we compare the intensity and kinematical maps for the different $^{12}$CO 3-2 data sets. Even though the long-baseline observation may be lacking flux in some regions, the cross-like structure is also present in the short-baseline data, pointing towards a real substructure and suggesting that no strong artefacts have been introduced in the imaging process. With three years having passed between the two observations, some time variations can, however, not be ruled out. It is puzzling that no similar structures are found in the $^{12}$CO 2-1 and $^{12}$CO 7-6 data. While the lack of features in $^{12}$CO 2-1 may be explained by temperature effects with the substructures becoming visible only at a certain height above the midplane, a similar pattern would at least be expected in $^{12}$CO 7-6, which traces even higher disc layers. Interaction with material from the environment of the disc could, however, wash out substructures. Moreover, $^{12}$CO 7-6 may be lacking flux in the outer disc regions. To get to the bottom of these peculiar substructures, it is crucial to obtain higher sensitivity data with a similar observational setup in the future.

On first look, the kinematics overall suggest an only mildly elevated disc: despite an inclination of $\sim 40\,^\circ$ only slight contributions from the back side of the disc are visible in $^{12}$CO and no contributions are seen in $^{13}$CO and C$^{18}$O. In the $^{12}$CO 7-6 kinematics, the central velocity seems to be off by a few $100\,\mathrm{m\,s^{-1}}$ from the systemic velocity of the source at $5.7\,\mathrm{km\,s^{-1}}$. This is also seen in the according channel map in Fig. 5.2 which seems 'S-shaped' as the south wing is bent upwards compared to the north wing. The central channel of the other lines on the other hand appears more symmetric. Assuming that $^{12}$CO 7-6 emission comes from a higher disc layer, the disc's surface may be distorted due to interactions with material from the environment. We analyse the kinematics in further detail in Sec. 5.3

Figure 5.4 presents normalized azimuthally averaged radial profiles of the integrated intensity for the lines of this analysis and the continuum emission. These profiles were obtained with the GOFISH package (Teague 2019) by shifting and stacking all line spectra to increase the SNR. This approach is based on the assumption that the disc is symmetric and Keplerian, which does not necessarily hold. Therefore, we compared the profiles to those obtained from simply azimuth-

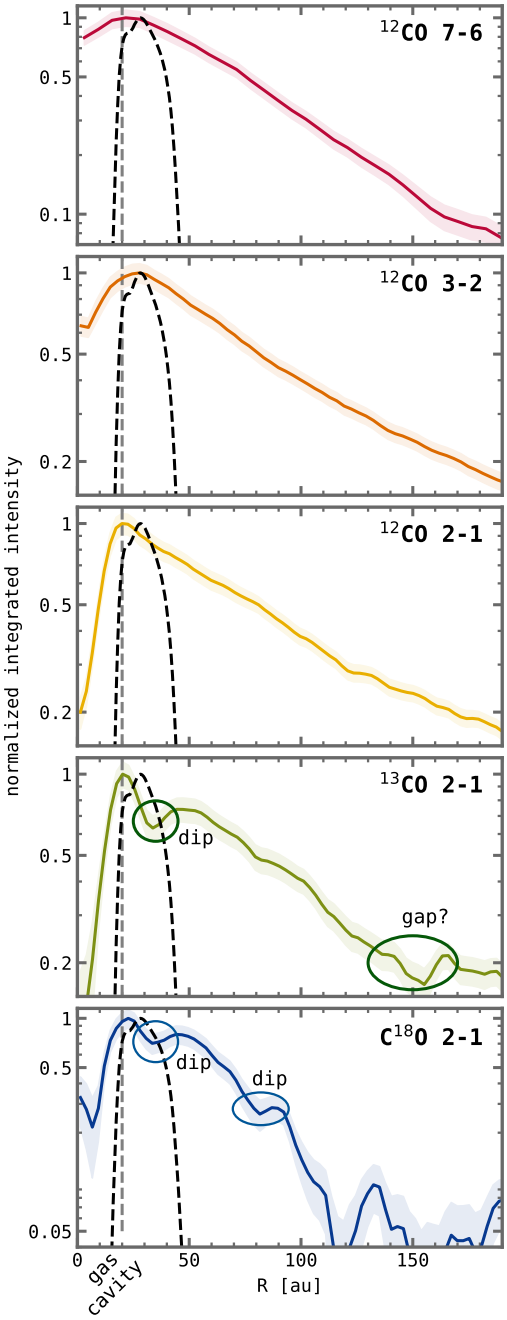


**Figure 5.4:** Azimuthally averaged and normalized radial integrated intensity profiles for the different CO lines. A radial profile of the Band 6 millimetre continuum is included as black dashed lines. The vertical grey dashed line marks the location inside which the gas emission rapidly drops (gas cavity). Some features of the profiles are annotated.

ally averaging the moment 0 maps, yielding similar results. By default, the widths of the annuli in the GOFISH package are given as one-fourth of the beam major axis. For the deprojection, we assume a disc geometry as obtained from the models presented in Sect. 5.3 and Table 5.4. The gas intensity significantly drops inside of $\sim 20$ au for all lines, thus just inside the dust cavity. We note the location of the drop as the gas cavity, but this represents an upper limit. To get a better estimate of the actual gas cavity, a more thorough analysis of the temperature structure across the cavity such as in Leemker et al. (2022) or a kinematical approach such as in Bosman et al. (2021) is required. In addition to the inner cavity, a prominent drop of emission is seen in $^{13}$CO and C$^{18}$O at $\sim 35$ au. This intensity drop coincides with the continuum emission and thus may be caused by continuum absorption rather than representing a gas gap. Another intensity drop is observed in C$^{18}$O around 85 au and in $^{13}$CO around 150 au, the C$^{18}$O emission is too noisy around this location. This dip corresponds to the gap tentatively detected in the channel maps. Continuum absorption is unlikely responsible for this substructure as it peaks around 200 au, but (particularly for C$^{18}$O) higher sensitivity data are needed to quantify a gas gap at these radii.

## 5.3 Analysis

### 5.3.1 Model setup

We use the DISCMINER code introduced in Izquierdo et al. (2021) to model the intensity channels (see Fig. 5.2) of the HD 100546 disc. In the following, we outline the basic modelling approach but refer the reader to Izquierdo et al. (2021) for the full details of the package. In the DISCMINER, parametric prescriptions are adopted to reproduce the intensity channel maps from molecular emission. The parameters used in this work are briefly summarized as follows (see Table 5.3).

To describe the orientation of the disc, we use the position angle PA, inclination $i$, and disc centre $(x_c, y_c)$. For the rotation velocity we adopt a Keplerian rotation, using the stellar mass $M_*$ and source systemic velocity $v_{sys}$ to describe the background velocity. The upper and lower emission surfaces are controlled by the height $z$ above and below the disc midplane. Here we use a power law with an exponential tapering. The line peak intensity, line width, and line slope across the disc radial and vertical extent are parameterized with simple power laws of the disc cylindrical coordinates $(R, z)$. For the peak intensity we select a combination of two power laws, describing the intensity profile inside and outside a radius $R_{break}$. By doing so, we are able to account for a decrease in intensity inside the gas cavity. For radii larger than the parameter $R_{out}$, the peak intensity is set to zero.

Subsequently, the DISCMINER is coupled with the Markov chain Monte Carlo (MCMC) random sampler EMCEE (Foreman-Mackey et al. 2013) to find those model parameters that best recover the intensity of the observed data cube. The different physical and morphological properties of the disc are thus modelled simultaneously to give a comprehensive view of the gas substructures and kinematics.

From the disc attributes, a model for the line profiles and data channels is generated. The modelled intensity $I_m$ is described by a generalized bell kernel

$$I_{\rm m}(R, z, v_{\rm ch}) = I_{\rm p} \left( 1 + |\frac{v_{\rm ch} - v_{\rm K^{l.o.s}}}{L_{\rm w}}|^{2L_{\rm s}} \right)^{-1} \tag{5.1}$$

as a function of the disc cylindrical coordinates $(R, z)$ and velocity channel $v_{\rm ch}$. $I_{\rm p}$ is the peak intensity, $L_{\rm w}$ half the line width at half power, $L_{\rm s}$ the line slope, and $v_{\rm K^{l.o.s}}$ the Keplerian line-of-sight velocity. The vertical coordinate $z$ is determined by the height of both the upper and the lower disc surface, thus each property except for $L_s$ has two descriptions. The contribution of the upper and lower emitting surfaces are merged into a single-line profile by selecting the highest intensity between bell profiles computed for both surfaces independently in each velocity channel and pixel.

**Table 5.3:** Parameterization adopted for the DISCMINER models in this work[(a)].

| Attribute | Parameterization |
|---|---|
| Orientation | $i$, PA, $x_{\rm c}, y_{\rm c}$ |
| Rotation velocity | $v_{\rm K} = \sqrt{GM_*/r^3} \cdot R$, $v_{\rm sys}$ |
| Emission surface | $z_{u,l} = z_{u0,l0}(R/D_0)^p \cdot \exp\left[-(R/R_{\rm t})^q\right]$ |
| Peak intensity | $I_{\rm p} = I_0(R/D_0)^{p0}(z/D_0)^q$, $R < R_{\rm break}$ |
| | $I_{\rm p} = I_0(R/D_0)^{p1}(z/D_0)^q$, $R > R_{\rm break}$ |
| | $I_{\rm p} = 0$, $R > R_{\rm out}$ |
| Line width | $L_{\rm w} = L_{\rm w0}(R/D_0)^p(z/D_0)^q$ |
| Line slope | $L_{\rm s} = L_{\rm s0}(R/D_0)^p$ |

**Notes.** [(a)] $D_0$ represents a normalization constant, set to 100 au, $R$ and $z$ are the disc cylindrical coordinates, and $r$ the spherical radius. $G$ is the gravitational constant, all other variables are left as free parameters.

### 5.3.2 Fitting procedure

To initialize the EMCEE sampler, we chose inclination, position angle, and stellar mass found by the models of Wölfer et al. (2023) and guessed the other parameters using the interactive prototyping tool of the DISCMINER, which allows to compare the morphology of the model and data channel maps as well as line profiles by eye. As a burn-in phase, the MCMC was then run with 256 walkers in two phases, first for 2000 steps and then for 5000 steps but using the fitting results from the previous run. Afterwards, we performed runs with the same number of walkers

and 10 000 steps until convergence was reached in all parameters. In each run, the posterior distribution was sampled from the last 1000 steps and used as initial parameters for the next step[3].

The noise of the data was taken into account in the fit: at each data pixel, the standard deviation of the residual intensities in line-free channels was calculated and adapted as a weighting factor for the likelihood function to be maximized by the sampler (see Izquierdo et al. 2021). To ensure that the noise of the individual pixels was approximately independent of their neighbouring pixels, we down-sampled the data with at least one beam while still ensuring that we had enough pixels left for the fit ($> 50$).

The HD 100546 disc has previously been proposed to be warped in the centre (Walsh et al. 2017). This could result in a temperature difference, potentially producing an elevation asymmetry, as it has been observed in CO emission of the Elias 2-27 disc (Paneque-Carreño et al. 2021). Moreover, the system is still surrounded by a diffuse envelope (Grady et al. 2001) and the infall of material from that envelope onto the disc could also result in such an asymmetry. To check for asymmetries between the blue- and redshifted sides of the disc, we conducted additional runs where only half of the channels of the according side were modelled instead of using the full cube. For $C^{18}O$ we switched off the lower surface in all runs since the channels appear to be very flat. Even though this is true also for $^{13}CO$, we ran models fitting for both surfaces and models where the lower surface was not included, yielding similar results. In the following, we will thus use the models where both surfaces were modelled. In the case of $^{12}CO$ 7-6, only the models that accounted for the blue- and redshifted side separately converged, however, they failed for the lower surface of the blueshifted side. To model the full cube, we therefore conducted additional runs with the lower surface switched off, which converged fine and are thus used in our following results.

### 5.3.3 Fitting Results

The best-fit parameters are summarized in Table 5.4 for the models fitting the full cube and in Tables 5.B.1 and 5.B.2 for the models fitting the blue- and redshifted side separately. The retrieved orientation of the disc is very similar in all models, resulting in a mean inclination $i$ and position angle PA of $42.71 \pm 1.48\,^\circ$ and $232.78 \pm 2.12\,^\circ$, respectively. A slightly larger, but still small scatter is found for the stellar mass ($2.14 \pm 0.15\,M_*$), which is relatively sensitive to changes in the model. For the Band 6 and Band 7 data, the systemic velocity is very close to the expected value of $5.7\,\mathrm{km\,s^{-1}}$, however, for the $^{12}CO$ 7-6 it is fitted as $5.4\,\mathrm{km\,s^{-1}}$. As mentioned before, this offset from the source velocity found in the literature (e.g., Walsh et al. 2014, 2017) can be seen in the channel and rotation maps. The trend of decreasing line width from $^{12}CO$ 7-6 to $C^{18}O$ is picked up by the DISCMINER. The radius $R_{\mathrm{break}}$, where a switch in the peak intensity profiles is happening, generally increases towards $C^{18}O$ (exception is $^{12}CO$ 3-2). This can be explained by the inner gas cavity ($< 20\,\mathrm{au}$) becoming more pronounced in the more optically thin lines. We note however, that $R_{\mathrm{break}}$ marks the point where the

[3]For the $^{12}CO$ 7-6 model we doubled the number of steps in all stages.

**Table 5.4:** Best-fit results of the modelling of the full cubes with the DISCMINER.

| Attribute | Parameter | Unit | $^{12}$CO 7-6 | $^{12}$CO 3-2 | $^{12}$CO 2-1 | $^{13}$CO 2-1 | C$^{18}$O 2-1 |
|---|---|---|---|---|---|---|---|
| Orientation | $i$ | $^\circ$ | 39.30 | 43.83 | 44.12 | 42.86 | 42.51 |
| | PA | $^\circ$ | 230.95 | 233.37 | 233.37 | 234.45 | 234.34 |
| | $x_\mathrm{c}$ | au | –0.44 | 10.29 | 2.11 | 0.23 | 2.61 |
| | $y_\mathrm{c}$ | au | –2.20 | –7.09 | –2.34 | –1.34 | –3.11 |
| Velocity | $M_*$ | $\mathrm{M}_\odot$ | 2.21 | 1.94 | 1.99 | 2.16 | 2.30 |
| | $\mathrm{v}_\mathrm{sys}$ | $\mathrm{km\,s^{-1}}$ | 5.38 | 5.65 | 5.65 | 5.64 | 5.64 |
| Upper surface | $z_0$ | au | 19.32 | 32.06 | 21.20 | 3.07 | 8.21 |
| | $p$ | - | 0.85 | 0.49 | 0.71 | 0.02 | 0.22 |
| | $q$ | - | 1.88 | 1.78 | 3.64 | 5.05 | 1.88 |
| | $R_\mathrm{t}$ | au | 292.86 | 303.21 | 324.06 | 212.80 | 161.45 |
| Lower surface | $z_0$ | au | - | 15.32 | 23.93 | 43.72 | - |
| | $p$ | - | - | 1.06 | 1.61 | 0.97 | - |
| | $q$ | - | - | 1.02 | 1.01 | 2.46 | - |
| | $R_\mathrm{t}$ | au | - | 265.38 | 147.78 | 20.98 | - |
| Intensity | $I_0$ | $\mathrm{Jy\,px^{-1}}$ | 7.04 | 5.56 | 0.21 | 0.06 | 0.009 |
| | $p_0$ | - | –0.97 | 0.79 | –0.08 | 0.97 | 0.94 |
| | $p_1$ | - | –1.40 | –0.58 | –0.88 | –0.41 | –2.46 |
| | $q$ | - | 0.83 | 0.59 | 0.55 | 0.32 | 0.001 |
| | $R_\mathrm{break}$ | au | 54.98 | 37.90 | 55.05 | 59.14 | 64.20 |
| | $R_\mathrm{out}$ | au | 322.04 | 372.79 | 369.84 | 326.29 | 253.61 |
| Line width | $L_\mathrm{W}$ | $\mathrm{km\,s^{-1}}$ | 2.01 | 1.03 | 0.66 | 0.29 | 0.02 |
| | $p$ | - | –0.90 | –0.73 | –0.59 | –0.80 | –1.28 |
| | $q$ | - | 0.44 | 0.13 | –0.002 | –0.11 | –0.87 |
| Line slope | $L_\mathrm{S}$ | - | 2.03 | 1.81 | 2.02 | 1.61 | 1.74 |
| | $p$ | - | 0.29 | 0.11 | 0.26 | 0.08 | –0.001 |

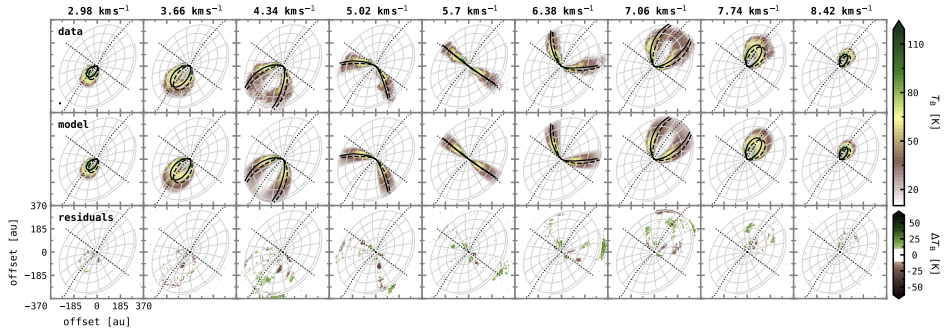


**Figure 5.5:** Examples of the intensity channels of $^{12}$CO 2-1 (top), shown in steps of four around the central channel, alongside the best-fit model obtained with the DISCMINER (middle) and the corresponding residuals (bottom). The iso-velocity curves of the upper and lower surfaces are overlaid as solid and dashed lines, respectively. The emitting surface and disc axes are plotted in the background as grey contours and dotted lines, respectively. The beam of the observation is indicated in the bottom left corner of the first panel.

intensity is maximal and not the actual cavity radius, and other effects (such as temperature) influence its location.

#### 5.3.3.1 Channel maps

In Fig. 5.5, we present a comparison of the data and best-fit model channels of $^{12}$CO 2-1 alongside the residuals obtained from subtracting the model from the data. The channels are shown in steps of four around the central channel. The according plots of the other lines are included in Appendix 5.C. The overall morphology of the data channels is well reproduced by the models, except for $^{12}$CO 7-6, where the lower surface could not be modelled properly.

The emission surfaces obtained from the models are overlaid as grey contours in the individual panels. For all lines, their morphology matches that of a rather flat and not very flared disc: the back side of the disc is barely visible and the azimuthal contours do not show any clear bending. While this is not unusual for $^{13}$CO and C$^{18}$O, it is puzzling that we do not see a stronger manifestation of the vertical structure in $^{12}$CO.

The surface of the disc is expected to become most visible in $^{12}$CO 7-6. In Fig. 5.C.2, we therefore plot the channels as a combination of the models fitting only half of the cube. While the emission surface on the blueshifted side is still showing a flat morphology, the redshifted side appears much more elevated and flared. A similar exercise for the other $^{12}$CO lines did not yield a significantly different emission surface compared to the one retrieved from the full cube. Another interesting point about the combined $^{12}$CO 7-6 plot is that it shows that the vertical structure itself can produce apparent wiggles in the channels, which are nicely retrieved by the model, especially for the blueshifted side.

The residuals of the different lines partly reach high values, suggesting that

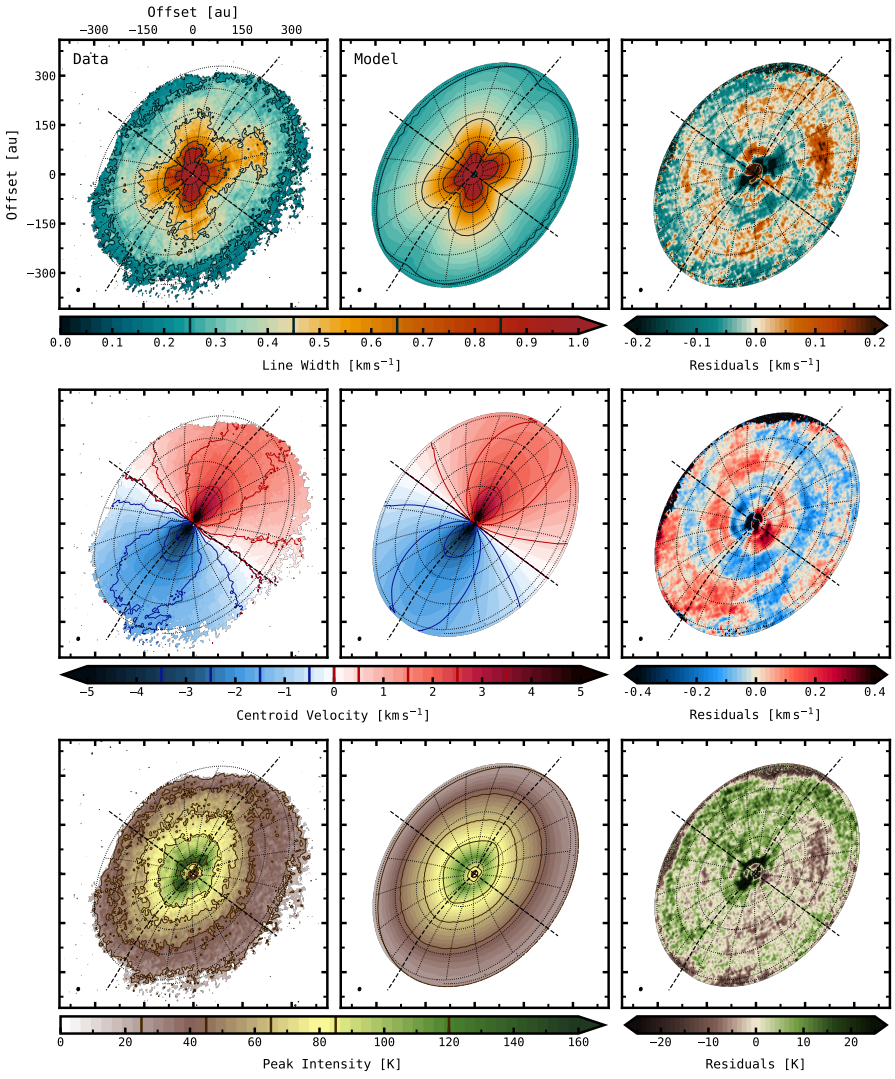


**Figure 5.6:** Observables extracted from the modelled line intensity, shown for $^{12}$CO 2-1 as an example. Displayed are the line widths (top), centroid velocities (middle), and peak intensities (bottom) for the data and best-fit model. The residuals, showing the differences between the data and model, are included in the last column. Some contour levels, indicated in the colour bars, are included to ease comparison. The emission surface and disc axes are plotted as dotted and dashed lines, respectively.

a smooth Keplerian model cannot fully reproduce the data. These deviations from Keplerian rotation can be used to unveil the mechanisms being at play, including massive planets but also other physical processes such as disc winds, hydrodynamical instabilities, or turbulence.

#### 5.3.3.2 Observables

From the line intensity profiles modelled by the DISCMINER, we extract three observables to search for substructures in the gas disc of HD 100546: the line width, centroid velocity, and peak intensity or brightness temperature. These are computed from Gaussian kernels which are fitted to both the data and the model and illustrated in Fig. 5.6 (left and middle panels) for the $^{12}$CO 2-1 line. The residuals resulting from the deviations of the data from the model are depicted in the right panels. The different observables can be used to trace various physical properties of the disc. The line width and peak intensity are shaped by both the gas temperature and density, the line width can additionally be used to trace turbulent motions. The gas motions which manifest in the kinematics are driven by dynamical, and often coupled, processes, including the gravitational influence of embedded (massive) bodies. Using the vertical emission structure together with the orientation of the disc as modelled by the DISCMINER, the observables can be deprojected onto the disc's reference frame and their substructures can be analysed in terms of location, magnitude, and extent.

## 5.4 Results

### 5.4.1 Kinematics

In Fig. 5.7 we show the centroid velocity residuals for all five lines, ordered from the brightest to the faintest. It is striking, that prominent spiral features are visible in all maps: in $^{12}$CO 7-6, a large coherent spiral runs from the inner disc around 50 au and 90 ° out to radii of 300 au, and possibly further, covering more than one full azimuth. In $^{12}$CO 3-2, similar features can be discerned, yet they are not as connected. In $^{12}$CO 2-1, which has a higher spatial resolution, the spiral seems to consist of several arms which are slightly more tightly wound than in $^{12}$CO 7-6. In $^{13}$CO and C$^{18}$O, the spirals become even more tightly wound. The anchoring point of the spiral substructures lies between 50 and 150 au and between 60 and 120 °.

To further analyse the spiral features we plot the binned residuals as radius versus azimuth in Fig. 5.8 and attempt to reproduce the morphology of the spirals (by eye) with different functional forms: an Archimedean or linear spiral

$$r = a + b\phi, \tag{5.2}$$

and a logarithmic spiral

$$r = ae^{b\phi}, \tag{5.3}$$

where $r$ is the radius and $\phi$ the polar angle of the spiral. In Fig. 5.7 we overlay the obtained linear spirals, the logarithmic spirals are presented in Fig. 5.D.1. The overall morphology of the spiral substructures is well represented by both parameterizations, however, the logarithmic spirals tend to deviate more from the features in the outer disc, while they better reproduce the bending in the inner disc than the linear spiral, which can by definition not account for that. Connected

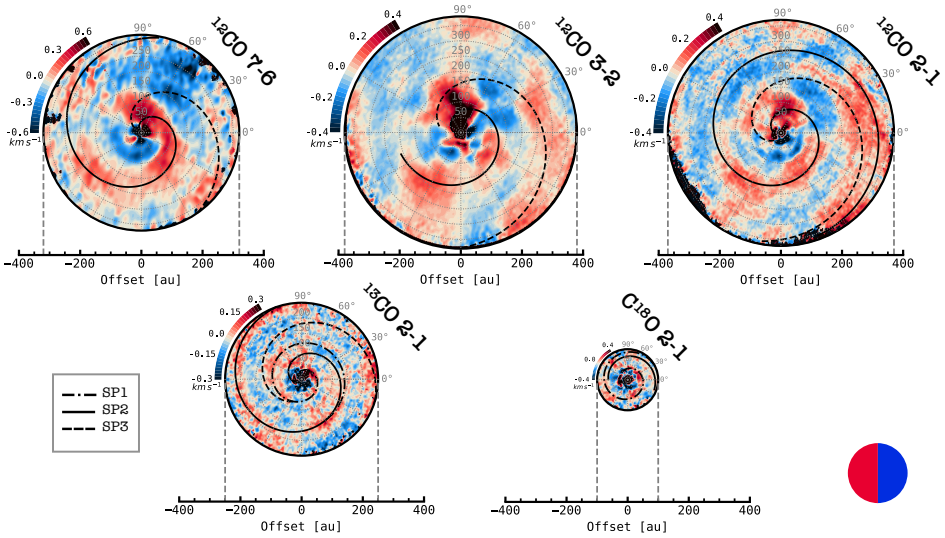


**Figure 5.7:** Centroid velocity residuals, shown for the five lines studied in this work. All lines exhibit extended spiral substructures. A linear (by-eye) parameterization of the spirals is overlaid as black lines. The spirals are labelled depending on their (increasing) radius as SP1, SP2, and SP3. The circle in the lower right corner indicates the blue- and redshifted sides of the disc.

to that, three linear spirals can account for the substructures seen in $^{13}$CO 2-1, but only two logarithmic spirals are needed to match the pattern. The different spirals are labelled as SP1, SP2, and SP3 depending on their radial locations (i.e., SP1 is the spiral closest in, SP3 the farthest). We note that the second spiral is not really visible as a connected structure in $^{12}$CO 7-6 but we have based this on the features seen in $^{12}$CO 2-1.

Comparing the three $^{12}$CO lines, it seems that a blue feature, separating the inner and outer parts of the spiral, is emerging more and more from $^{12}$CO 2-1 to $^{12}$CO 7-6. This suggests that other mechanisms shaping the kinematics may be coming into play, for example, interactions with the discs's environment (such as infall) which are adding a large velocity dispersion.

The parameters of the individual spiral prescriptions are presented in Table 5.5. They can be used to compute the opening angle or pitch angle $\beta$ of the spirals with

$$\tan\beta = \left|\frac{dr}{d\phi}\right| \cdot \frac{1}{r}. \tag{5.4}$$

This results in a constant pitch angle for the logarithmic and a radially varying one for the linear spirals. The pitch angles are plotted in Fig. 5.9. For the linear spirals, the pitch angles are relatively small in the outer disc regions but rapidly increase inside of $\sim 50$ au. The constant pitch angles found from the logarithmic spirals have values below 20 °. In both cases, the pitch angles decrease from $^{12}$CO 7-6 to C$^{18}$O 2-1 and from SP3 to SP1, which is in agreement with the predictions of Juhász & Rosotti (2018) from modelling of thermal stratification.

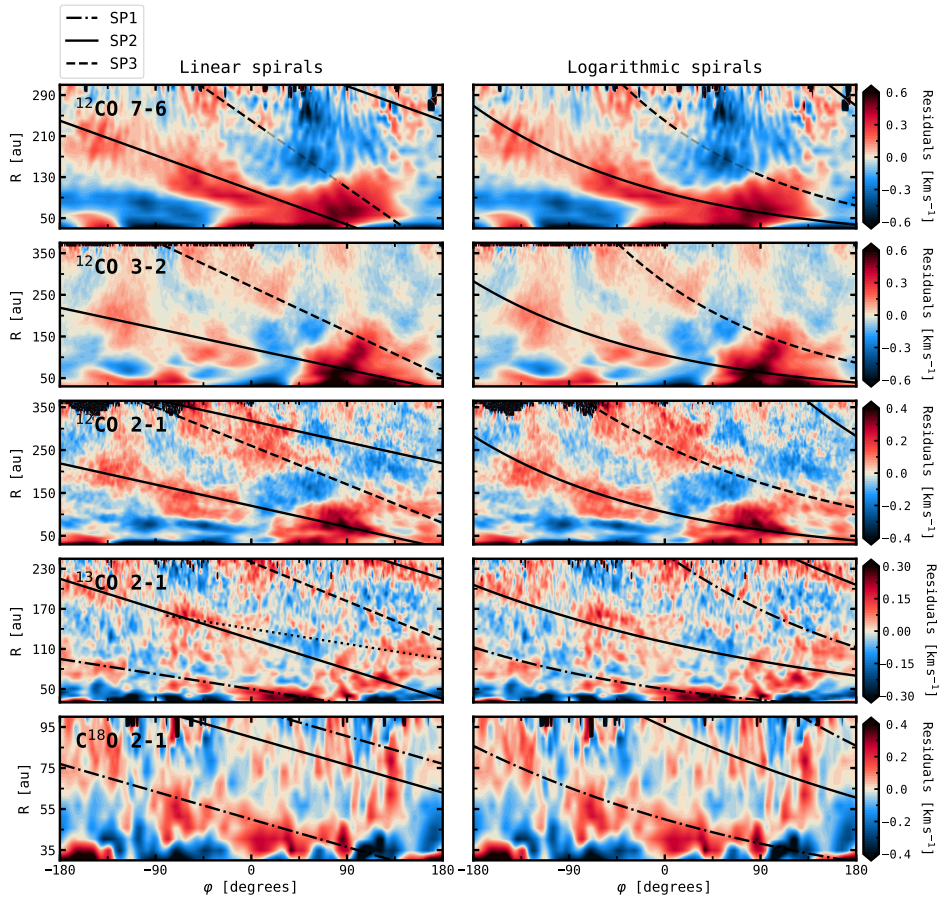


**Figure 5.8:** Azimuthal deprojection of the centroid velocity residuals of the five lines, shown with overlaid linear (left) and logarithmic (right) spirals. The spirals are labelled depending on their (increasing) radius as SP1, SP2, and SP3.

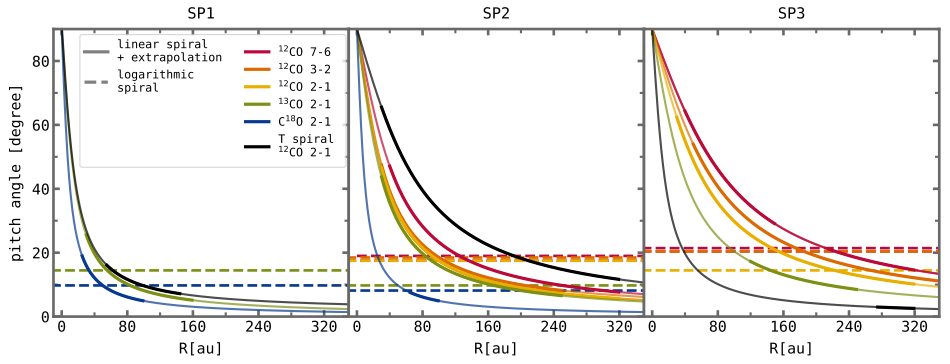


**Figure 5.9:** Pitch angles of the spirals observed in the kinematics (and peak intensity of $^{12}$CO 2-1), obtained from a linear and a logarithmic prescription.

**Table 5.5:** Parameters to reproduce the spirals (by eye) with linear and logarithmic functions.

| | | Parameter | $^{12}$CO 7-6 | $^{12}$CO 3-2 | $^{12}$CO 2-1 | $^{13}$CO 2-1 | C$^{18}$O 2-1 | $^{12}$CO 2-1 $T_{\rm B}$ |
|---|---|---|---|---|---|---|---|---|
| Linear | SP1 | a (au) | - | - | - | 50 | 50 | 100 |
| | | b ($^\circ$ au$^{-1}$) | - | - | - | –0.25 | –0.15 | –0.25 |
| | SP2 | a | 105 | 120 | 120 | 125 | 90 | 90 |
| | | b | –0.75 | –0.55 | –0.55 | –0.5 | –0.15 | –1.15 |
| | SP3 | a | 240 | 270 | 260 | 240 | – | 290 |
| | | b | –1.45 | –1.2 | –1.0 | –0.65 | – | –0.25 |
| Logarithmic | SP1 | a (au) | - | - | - | 50 | 50 | - |
| | | b ($^\circ$ au$^{-1}$) | - | - | - | –0.0045 | –0.003 | - |
| | SP2 | a | 100 | 105 | 105 | 120 | 95 | - |
| | | b | –0.0055 | –0.0055 | –0.0055 | –0.003 | –0.0025 | - |
| | SP3 | a | 240 | 280 | 260 | - | - | - |
| | | b | –0.0065 | –0.0065 | –0.0045 | - | - | - |

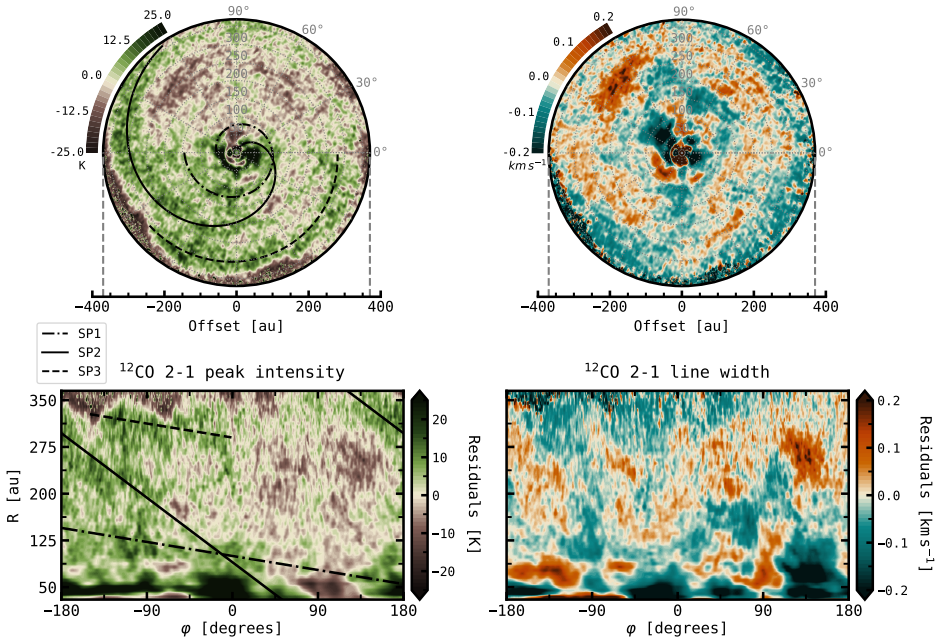


**Figure 5.10:** Peak intensity (left) and line width (right) residuals of $^{12}$CO 2-1. Shown are the deprojected maps (top) and an azimuthal deprojection (bottom). In the peak intensity, three parameterizations of a linear spiral are overlaid.

### 5.4.2 Peak intensities and line widths

The residuals of the peak intensity and line widths are displayed in the Appendix in Figs. 5.E.1 and 5.E.2, again shown ordered from the brightest to the faintest line. The substructures in the peak intensity and line width are less clear than in the kinematics and no coherent spiral structures can be discerned. In $^{12}$CO 7-6, the upper half of the disc (corresponding to the southwest side of the disc in disc coordinates) happens to be colder while the lower half is hotter. This corresponds to the brightness asymmetry mentioned before, which is seen in the channels. The line widths on the other hand are increased in the upper half of the disc, but they are decreased in the lower side. Together, this may suggest that the surface density is larger on the upper (south) side, thus broadening the line width and at the same time lowering the temperature. The additional material could be a result of infall processes, which do not only increase the density but also add a large velocity dispersion, which affects the shape of the line profile.

In $^{12}$CO 3-2, peculiar wing- and cross-like structures are present in both the peak intensity and line width residuals, showing a very similar pattern, yet with opposite signs (i.e., enhanced temperatures correspond to decreased line widths). Another prominent feature is a localized temperature enhancement around 150 au and 60 °, which corresponds to the spot already seen in the channel maps. The features in $^{12}$CO 3-2 are very hard to interpret and better resolution data (including

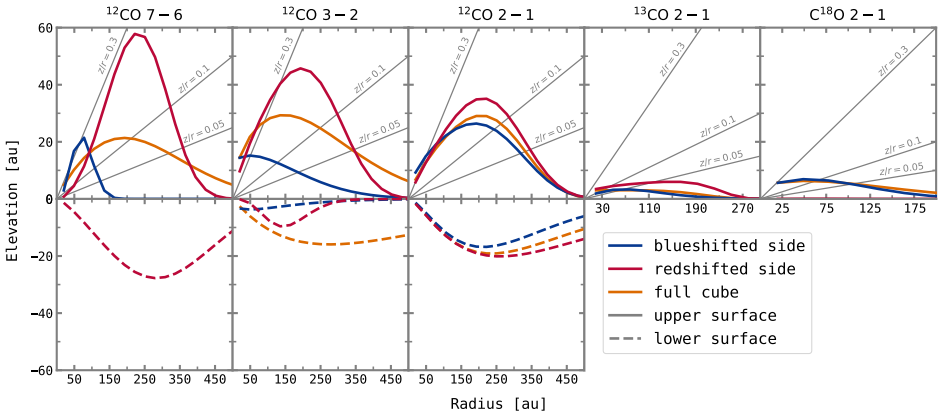


**Figure 5.11:** Upper (top) and lower (bottom) emission surfaces of the five molecular lines, shown for the fits of the full cube and the fit of the blue- and redshifted sides only.

the short and long baseline observations with the same setup) are needed to make any quantitative remarks. Similarly, higher sensitivity data are needed for $^{13}$CO and C$^{18}$O, which show cross-like patterns in the line width residuals, resulting from the missing fit of the lower surface.

Somewhat clearer substructures can be discerned in $^{12}$CO 2-1, for which we show the projected and polar-deprojected maps in Fig. 5.10. In the peak intensity, three tentative spiral- or arc-like structures are visible, which we reproduce with the linear function. The parameters and pitch angles obtained for these spirals are included in Table 5.5 and Fig. 5.9. We note that it is difficult to clearly disentangle the patterns seen in the $^{12}$CO 2-1 peak-intensity residuals and their connection. Therefore, the parameterizations of the temperature spirals should be treated with caution. Furthermore, a prominent ring of enhanced line widths can be distinguished between $\approx 125 - 330$ au, showing a particularly bright region between 100–150 °. The ring co-locates with both low and high temperatures and it is thus difficult to say if the lines are broadened by temperature effects or density enhancements. The localized region on the other hand coincides with a low-temperature spot and may be tracing a region of dense gas material or turbulent motions rather than temperature.

### 5.4.3 Emission heights

In Fig. 5.11, we present the emission layers of the upper and, in case of $^{12}$CO, lower surfaces of the disc, extracted from the DISCMINER models. Here we plot the profiles obtained from runs fitting for the full cube (orange) as well as the blue- and redshifted sides only. The curves show that while the optically thick $^{12}$CO emission is coming from more elevated disc layers, particularly in the higher transitions, $^{13}$CO and $^{18}$CO originate from similar layers that are very close to the midplane. Furthermore, a clear asymmetry between the red- and blueshifted side

is revealed, which becomes particularly strong for $^{12}$CO 7-6 and $^{12}$CO 3-2: the emission of the redshifted side of the disc is coming from much higher disc layers ($\sim$ 30 au difference for $^{12}$CO 7-6 and $^{12}$CO 3-2) than that of the blueshifted side, which can already be seen in the channel maps (see for example Fig. 5.C.2). Such an asymmetry has been detected before only for the Elias 2-27 disc, a massive and gravitationally unstable disc, that may be affected by infall or an inner warp (Paneque-Carreño et al. 2021, 2022).

### 5.4.4 Azimuthal averages

In Fig. 5.12, we plot the azimuthally averaged residuals, including both the azimuthal and vertical velocity perturbations aside from the line width and peak intensity deviations. The former two are obtained by using either the simple subtraction of the DISCMINER model from data or subtracting absolute values. The derivation of the azimuthal and vertical velocities is detailed in Izquierdo et al. in submission. In Fig. 5.12, we mark the locations where planets have previously been proposed as well as the centres of the two observed dust rings (B28 and B200). We further annotate some trends seen in the profiles such as the sign of the velocity gradient in the azimuthal perturbations (tracing pressure minima and maxima), upwards and downwards meridional flows in the vertical perturbations, and local minima or maxima in the line width and peak intensity. We discuss some of the trends seen in the averages in the following, however, we note that their computation is based on the assumption of axisymmetry, which does not necessarily hold. In fact, the spiral structures seen in the kinematics suggest the perturbations to be non-symmetric. Nevertheless, the curves are still useful to get an indication of some general trends.

At the location of the dust rings, negative velocity gradients are seen in all lines except $^{12}$CO 7-6, tracing pressure bumps which can account for the formation of the rings. In this context, the more optically thin lines tracing regions closer to the midplane can better constrain the underlying density profile than the optically thick lines which are affected by the temperature. Thus, it is not surprising that $^{12}$CO 7-6 is showing an opposite trend. Inside the inner dust cavity, a strong positive gradient is present and downward meridional flows indicate the gas material falling into the cavity. However, close to the star, beam smearing and optical depth effects are becoming significant, resulting in large errors, and inside of $\sim$ 25 au the profiles have to be treated with caution. For the same reason, we are not able to draw any conclusions on the features seen around the innermost planet candidate at $\sim$ 15 au. Around the location of the second planet candidate at $\sim$ 53 au, both $^{13}$CO and C$^{18}$O show strong positive gradients, supporting the presence of a gas gap that indeed may be carved by a massive companion. Again, an opposite trend is visible in $^{12}$CO but as mentioned above, $^{13}$CO and C$^{18}$O are more likely to trace pressure minima related to a low gas density. Just inside the planet candidate's location, downward meridional flows are seen in all lines, further supporting the presence of a companion. Moreover, there are line width minima (in $^{12}$CO) that align well with the meridional flows. The brightness temperature shows strong fluctuations inside of $\sim$ 100 au, which are hard to put into context with the other

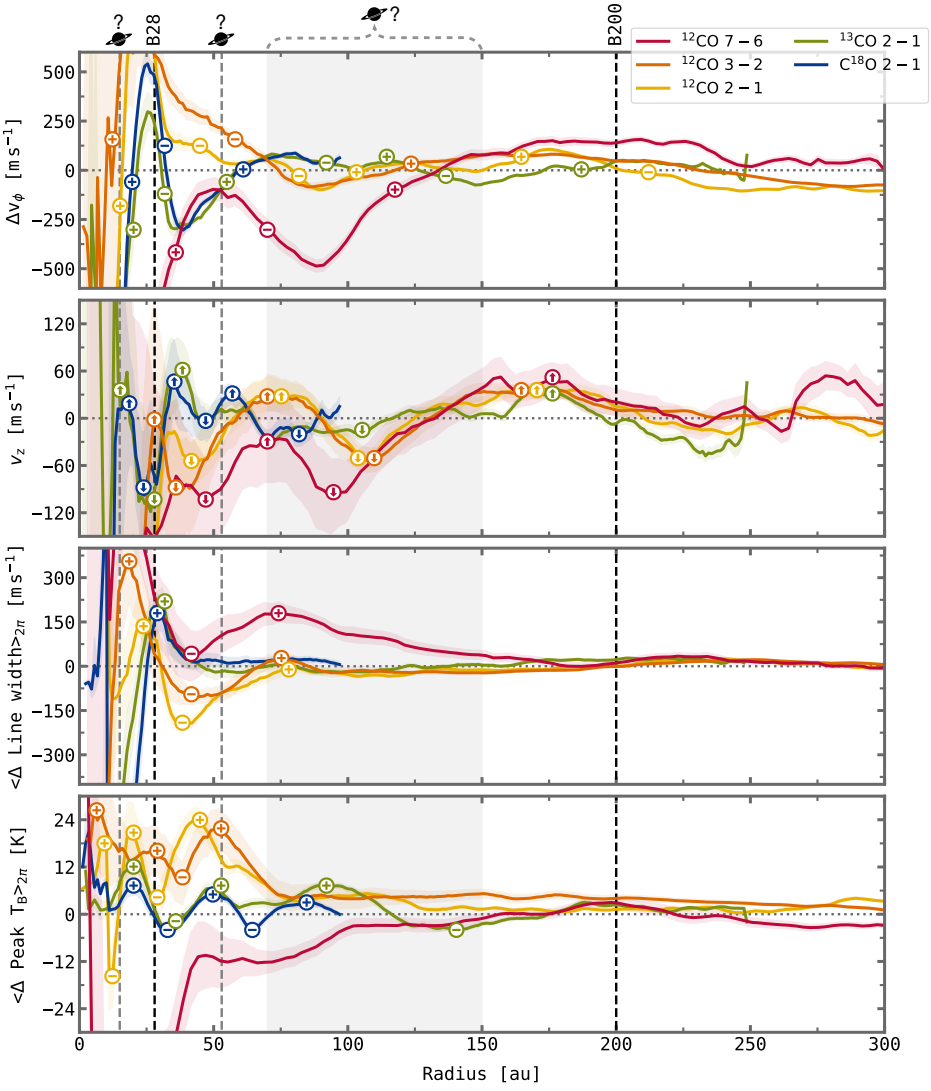


**Figure 5.12:** Azimuthally averaged profiles of the azimuthal and vertical velocity (top two panels), line width (third panel), and peak intensity (lower panel) residuals, shown for all five lines. The centres of the dust rings and locations of previously proposed planets are marked by dashed lines and a shaded region. In the top panel, the sign of the velocity gradient is indicated with plus and minus signs. In the second row, meridional flows hinting at gas moving away from and towards the disc midplane are highlighted as up and down arrows. Local line width and temperature maxima and minima are indicated with plus and minus signs.

substructures and their origin cannot really be assessed.

Except for $C^{18}O$, for which the emission is not as extended, positive azimuthal velocity gradients and significant downward meridional flows are present in all molecular tracers between 90–125 au, which coincides with the dust gap found by Fedele et al. (2021), the third proposed location of a planet candidate, the location of the bright spot in $^{12}$CO 3-2, and the gap seen in the radial profile of $^{13}$CO. For most of the radii, where the ring of enhanced line widths is observed in $^{12}$CO 2-1 (see Fig. 5.10), a negative azimuthal velocity gradient is found, supporting that we are indeed tracing a gas ring.

## 5.5 Discussion

### 5.5.1 On the planet candidate at 50 au

All molecular tracers analysed in this study exhibit extended spiral structures in the kinematical residuals, which we reproduce (by eye) with linear and logarithmic functions (Figs. 5.7, 5.8). Their consistency suggests them to be real features tracing a common origin. The pitch angles of the linear spirals show small values at most radii but rapidly increase inside of ∼50 au. Such a behaviour is consistent with Lindblad-resonance-driven spiral wakes of a massive embedded companion (e.g., Ogilvie & Lubow 2002; Rafikov 2002; Bae & Zhu 2018a,b), which tend to increase only close to the location of the planet. The logarithmic spirals on the other hand show constant pitch angles below 20 °, which are more consistent with tightly wound spirals excited by a planet through buoyancy resonances (Bae et al. 2021). In both cases, the spirals support the presence of a companion inside of ∼ 50 au and therefore provide additional evidence for the planet candidate HD 100546 b, even though also the candidate HD 100546 c could in principle explain the formation of the spirals. Furthermore, the possibility of a binary rather than a planetary companion, as invoked by Norfolk et al. (2022), cannot be ruled out with the present data. The HD 100546 disc has previously been suggested to be warped in the centre (Walsh et al. 2017), and a binary companion would provide a good explanation for both the extended spiral structures and the misaligned inner disc. Hydrodynamical simulations are needed to further distinguish between the Lindblad and buoyancy scenario and to make predictions on the companion mass and location.

While velocity spirals do not necessarily align with spiral features in the peak intensity, it is still puzzling that except for $^{12}$CO 2-1, no counterpart of the kinematical spirals is found. Both in TW Hydra (Teague et al. 2019b, 2022a,b) and CQ Tau (Wölfer et al. 2021), temperature spirals have been observed that overlap at least partly with the spirals in the velocity residuals, suggesting that there may be a physical mechanism behind their connection. In the companion scenario, the spiral density waves lead to an increase in surface density and thus to a higher CO opacity. The $\tau = 1$ layer is moved to a larger altitude, where the temperature is generally higher, resulting in the observed spiral substructure in the gas temperature (Phuong et al. 2020a,b). The lack of temperature features in HD 100546 is therefore unexpected, however, velocity spirals are more easily detected than

those in the peak brightness temperature. The absence could therefore result from sensitivity effects and needs to be further investigated in the future.

Aside from dynamical interactions with a companion, spiral structures can also be a signpost of gravitational instability (GI; e.g., Rice et al. 2003). In that case, the pitch angles are expected to be comparable for the surface and the midplane layers, which are heated by shocks. On the other hand, the pitch angle is expected to increase towards the surface layers in the companion scenario if the disc is passively heated with a positive vertical temperature gradient (Juhász & Rosotti 2018). The spirals in HD 100546 indeed become more tightly wound towards the midplane, supporting the predictions by Juhász & Rosotti (2018) and dynamical interactions rather than GI as the underlying mechanism.

### 5.5.2 On the planet candidate between 70–150 au

To explain the ringed substructures in the dust, a planet orbiting at large separations between 70–150 au has previously been proposed (Walsh et al. 2014; Pinilla et al. 2015; Fedele et al. 2021; Pyerin et al. 2021). In this region, we observe vertical motions directed down towards the midplane around $\sim 110$ au in $^{12}$CO 3-2, $^{12}$CO 2-1, and $^{13}$CO 2-1, and around $\sim 95$ au in $^{12}$CO 7-6 (Fig. 5.12, panel two). This shift is not surprising as the lines trace different heights in the disc which are governed by different physical and chemical processes. Such meridional flows are commonly associated with forming planets and similar motions have been observed before by Teague et al. (2019a), possibly tracing a depletion of gas material carved by an embedded companion. The presence of a gas gap around 90–150 au is further supported by the positive sign of the azimuthal velocity gradient at these radii (Fig. 5.12), and tentative dips of emission in the azimuthally averaged radial intensity profiles of $^{13}$CO ($\sim 150$ au) and C$^{18}$O ($\sim 85$ au) (Fig. 5.4). Lastly, a bright, localized spot stands out in the velocity channels and peak intensity map of $^{12}$CO 3-2 around 125 and 150 au, respectively. Altogether, these features strongly support the presence of a massive planet in the outer disc. However, higher sensitivity data at high resolutions are needed to confirm the robustness of the substructures. Moreover, a comparison with hydrodynamical models is crucial to understand if they can indeed be explained by a massive embedded body.

### 5.5.3 Origin of the asymmetry in emission heights

The CO emission of HD 100546 is marked by an asymmetry between the blue- and redshifted halves of the disc, which is especially pronounced in $^{12}$CO 7-6 and $^{12}$CO 3-2 (Fig. 5.11). Such an asymmetry has previously been detected only for the Elias 2-27 disc (Paneque-Carreño et al. 2021, 2022). One explanation could be given by infall onto the redshifted side of the disc. Infalling material results in an increase of the surface density, and thus the emission becomes optically thick in higher disc layers. Moreover, the temperature is altered as shocks will heat the layers on which the material is accreted (Hennebelle et al. 2017). Observations of scattered light have indeed revealed that the disc is surrounded by a diffuse envelope (Grady et al. 2001; Ardila et al. 2007). Another scenario that may account for the asymmetry

is the presence of a warped inner disc casting a shadow over part of the outer disc, shielding it from stellar radiation and thus resulting in an azimuthal variation of the temperature, which has an immediate effect on the vertical structure of the disc. The northeast side of the disc indeed appears to be brighter, which is in agreement with a shadowing misaligned disc. A warped inner disc can in principle be triggered by binary interactions or a misaligned planet (e.g., Nealon et al. 2018) but also the infall of material may produce such a structure (Bate et al. 2010; Sakai et al. 2019).

## 5.6 Summary

In this work, we have modelled the molecular line emission of five CO lines observed with ALMA in the circumstellar disc around HD 100546. Our main results are summarized as follows.

- Extended spiral features are resolved in the kinematics of all five lines. The peak intensity also shows indications of spirals but only in $^{12}$CO 2-1, likely due to limited sensitivity for the other lines. A ring and bright region of enhanced line widths are seen in the line width residuals of $^{12}$CO 2-1.
- The spirals are well reproduced by a linear and/or a logarithmic function and show small pitch angles that are consistent with Lindblad or Buoyancy spirals driven by a companion.
- A rapid increase of the pitch angles inside of $\sim 50$ au suggests an upper limit for the companion location around this radius, which is consistent with the planet candidate HD 100546 b or HD 100546 c but may point to a binary companion rather than a planet as suggested by Norfolk et al. (2022).
- Several indications for a companion at larger separations (90–150 au) are present: meridional flows towards the midplane and pressure minima around this region suggest a gas-depleted ring that may be carved by an unseen planet. In the radial curves of the integrated intensity of $^{13}$CO 2-1 and C$^{18}$O 2-1, tentative gas gaps are visible at 150 and 85 au, respectively, but they need to be confirmed with higher sensitivity data. Altogether, these features coincide with the dust gap observed by Fedele et al. (2021).
- The emission from the redshifted side appears more elevated compared to the blueshifted side of the disc. Such an asymmetry may result from infalling material on one side of the disc, thus increasing the density and lifting the optically thick emission layer. Temperature effects resulting from a warped inner disc casting a shadow over the disc represent an alternative explanation.

High-sensitivity multi-line and multi-isotopologue data (of different molecules) taken at high spectral and spatial resolution are of paramount importance to probe the full vertical and radial extent of protoplanetary discs. Mapping out their structures and kinematics may enable us to distinguish different disc-shaping mechanisms, including planet–disc interactions, and to link their properties to those of the mature exoplanet populations.

## Acknowledgements

This paper makes use of the following ALMA data: 2011.0.00863.S, 2015.1.00806.S, 2016.1.00344.S, and 2018.1.00141.S. ALMA is a partnership of ESO (representing its member states), NSF (USA) and NINS (Japan), together with NRC (Canada) and NSC and ASIAA (Taiwan) and KASI (Republic of Korea), in cooperation with the Republic of Chile. The Joint ALMA Observatory is operated by ESO, auI/NRAO and NAOJ.

# Appendix

## 5.A Comparison of the $^{12}$CO 3-2 data sets

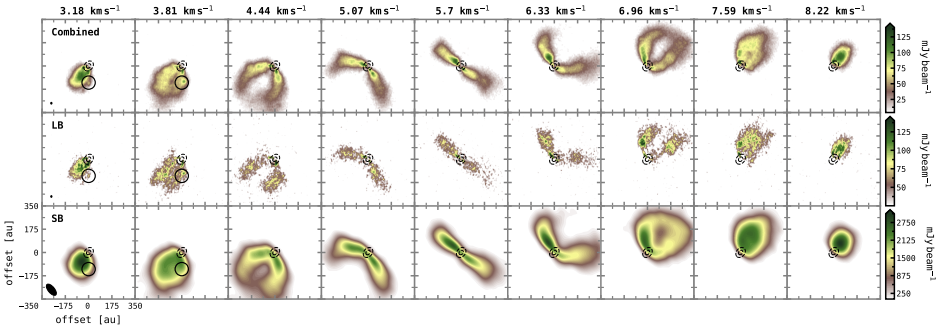


**Figure 5.A.1:** Comparison of the different $^{12}$CO 3-2 data sets, with the combined data in the top row, the long-baseline data in the middle row, and the short-baseline data in the bottom row. Shown are the channels in steps or three from the central channel and for a velocity resolution of 210 m s$^{-1}$. The inner millimetre continuum ring is overlaid as dashed contours. A localized feature is seen in some of the channels within the solid circle. The beam of the observation is indicated in the bottom left corner of the first panel of each row.

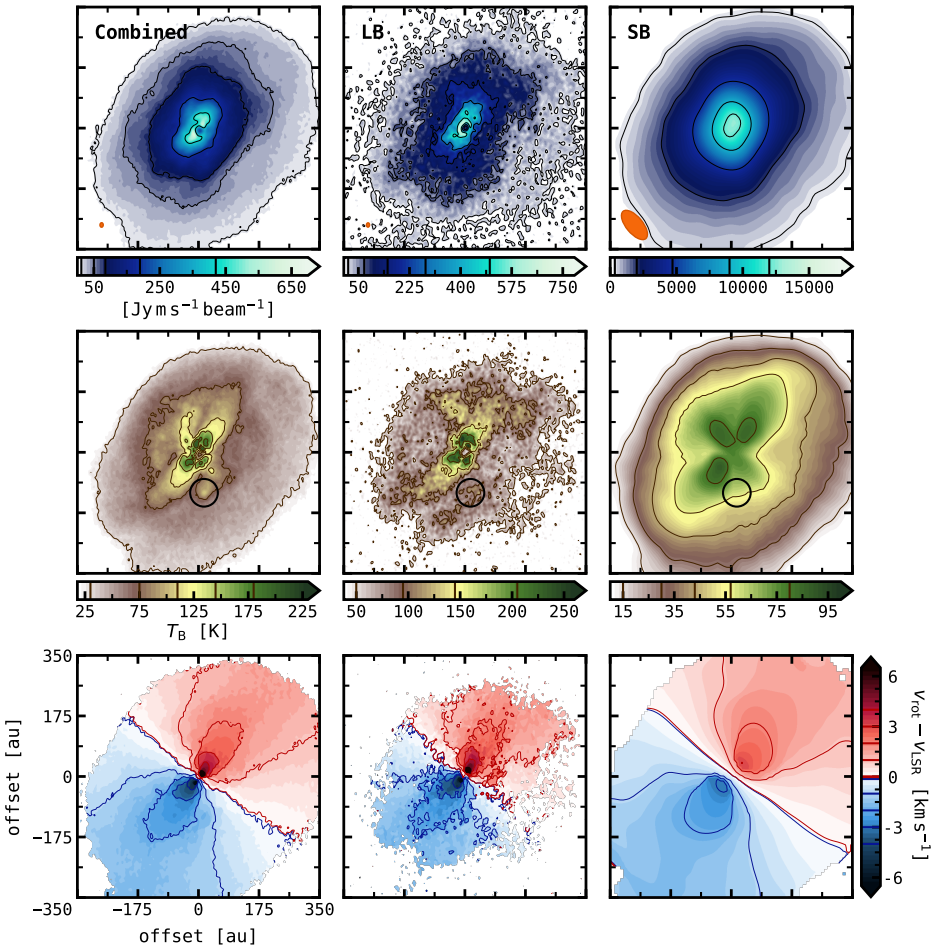


**Figure 5.A.2:** Comparison of the different $^{12}$CO 3-2 data sets, with the combined data in the left column, the long-baseline data in the middle column, and the short-baseline data in the right column. Shown are the integrated intensity (top), peak intensity (middle), and line-of-sight velocity (bottom). A localized feature is seen within the solid circle. Some contours are overlaid and their levels are indicated in the colour bars. The beam of the observation is shown in the bottom left corner of the first-row panels.

## 5.B Best-fit parameters blue- and redshifted sides

**Table 5.B.1:** Best-fit results of the modelling of the blueshifted channels with the DISCMINER.

| Attribute | Parameter | Unit | $^{12}$CO 7-6 | $^{12}$CO 3-2 | $^{12}$CO 2-1 | $^{13}$CO 2-1 | C$^{18}$O 2-1 |
|---|---|---|---|---|---|---|---|
| Orientation | $i$ | $^\circ$ | 41.88 | 42.06 | 44.06 | 41.88 | 42.06 |
| | PA | $^\circ$ | 230.73 | 233.54 | 234.40 | 234.63 | 233.94 |
| | $x_\mathrm{c}$ | au | 0.45 | 4.29 | 3.11 | 0.08 | 3.12 |
| | $y_\mathrm{c}$ | au | 0.63 | –6.32 | –1.37 | –1.42 | –3.47 |
| Velocity | $M_*$ | $\mathrm{M}_\odot$ | 2.12 | 1.99 | 2.12 | 2.25 | 2.40 |
| | $\mathrm{v}_\mathrm{sys}$ | $\mathrm{km\,s^{-1}}$ | 5.41 | 5.64 | 5.70 | 5.66 | 5.68 |
| Upper surface | $z_0$ | au | 146.40 | 17.65 | 21.94 | 7.80 | 10.60 |
| | $p$ | - | 2.38 | 0.12 | 0.54 | 0.83 | 0.38 |
| | $q$ | - | 2.27 | 1.78 | 3.44 | 1.65 | 2.02 |
| | $R_\mathrm{t}$ | au | 68.74 | 224.98 | 324.88 | 101.50 | 121.83 |
| Lower surface | $z_0$ | au | 0.0 | 5.97 | 19.65 | 31.72 | - |
| | $p$ | - | 0.06 | 0.30 | 1.63 | 1.14 | - |
| | $q$ | - | 5.22 | 1.21 | 1.18 | 2.40 | - |
| | $R_\mathrm{t}$ | au | 116.38 | 149.38 | 161.36 | 21.41 | - |
| Intensity | $I_0$ | $\mathrm{Jy\,px^{-1}}$ | 1.23 | 0.47 | 0.20 | 0.08 | 0.008 |
| | $p_0$ | - | –0.27 | 0.48 | –0.08 | 0.65 | 0.81 |
| | $p_1$ | - | –0.90 | –0.27 | –0.83 | –0.11 | –2.49 |
| | $q$ | - | 0.007 | 0.47 | 0.56 | 0.41 | 0.001 |
| | $R_\mathrm{break}$ | au | 55.14 | 39.67 | 59.18 | 59.69 | 65.16 |
| | $R_\mathrm{out}$ | au | 349.22 | 393.55 | 388.75 | 289.24 | 253.58 |
| Line width | $L_\mathrm{W}$ | $\mathrm{km\,s^{-1}}$ | 0.93 | 1.09 | 0.77 | 0.20 | 0.08 |
| | $p$ | - | –0.55 | –0.66 | –0.62 | –0.94 | –1.21 |
| | $q$ | - | 0.005 | 0.09 | 0.06 | –0.19 | –0.44 |
| Line slope | $L_\mathrm{S}$ | - | 2.05 | 1.74 | 2.01 | 1.62 | 1.80 |
| | $p$ | - | 0.21 | 0.14 | 0.23 | 0.07 | 0.03 |

**Table 5.B.2:** Best-fit results of the modelling of the redshifted channels with the DISCMINER.

| Attribute | Parameter | Unit | $^{12}$CO 7-6 | $^{12}$CO 3-2 | $^{12}$CO 2-1 | $^{13}$CO 2-1 | C$^{18}$O 2-1 |
|---|---|---|---|---|---|---|---|
| Orientation | $i$ | $^\circ$ | 45.26 | 41.65 | 44.46 | 43.54 | 41.14 |
| | PA | $^\circ$ | 226.83 | 230.16 | 232.74 | 234.05 | 234.17 |
| | $x_\mathrm{c}$ | au | –7.22 | 7.93 | 1.12 | 0.28 | –0.46 |
| | $y_\mathrm{c}$ | au | 1.61 | –8.96 | –3.29 | –2.09 | –3.12 |
| Velocity | $M_*$ | $\mathrm{M}_\odot$ | 1.84 | 2.18 | 2.04 | 2.16 | 2.38 |
| | $\mathrm{v}_\mathrm{sys}$ | $\mathrm{km\,s^{-1}}$ | 5.39 | 5.62 | 5.62 | 5.62 | 5.62 |
| Upper surface | $z_0$ | au | 19.29 | 33.91 | 23.64 | 5.57 | 12.13 |
| | $p$ | - | 2.02 | 0.78 | 0.87 | 0.29 | 3.78 |
| | $q$ | - | 3.44 | 3.52 | 3.47 | 7.28 | 1.12 |
| | $R_\mathrm{t}$ | au | 269.93 | 299.48 | 313.99 | 234.89 | 21.46 |
| Lower surface | $z_0$ | au | 11.82 | 21.17 | 27.43 | 2.52 | - |
| | $p$ | - | 1.34 | 3.26 | 1.61 | 0.23 | - |
| | $q$ | - | 2.48 | 1.67 | 0.87 | 3.07 | - |
| | $R_\mathrm{t}$ | au | 362.94 | 95.97 | 128.54 | 177.59 | - |
| Intensity | $I_0$ | $\mathrm{Jy\,px^{-1}}$ | 7.63 | 0.52 | 0.21 | 0.05 | 0.009 |
| | $p_0$ | - | –1.22 | 0.97 | 0.06 | 0.90 | 1.28 |
| | $p_1$ | - | –2.10 | –0.80 | –0.89 | –0.61 | –2.40 |
| | $q$ | - | 0.67 | 0.45 | 0.50 | 0.30 | 0.001 |
| | $R_\mathrm{break}$ | au | 56.69 | 40.33 | 50.56 | 61.69 | 60.35 |
| | $R_\mathrm{out}$ | au | 339.92 | 398.23 | 369.69 | 337.93 | 254.15 |
| Line width | $L_\mathrm{W}$ | $\mathrm{km\,s^{-1}}$ | 0.93 | 0.86 | 0.63 | 0.34 | 0.06 |
| | $p$ | - | –0.89 | –0.63 | –0.54 | –0.67 | –1.22 |
| | $q$ | - | 0.12 | 0.01 | 0.02 | –0.07 | –0.19 |
| Line slope | $L_\mathrm{S}$ | - | 2.22 | 1.77 | 1.99 | 1.59 | 1.69 |
| | $p$ | - | 0.32 | 0.20 | 0.27 | 0.09 | 0.07 |

## 5.C Comparison of the data and model channels

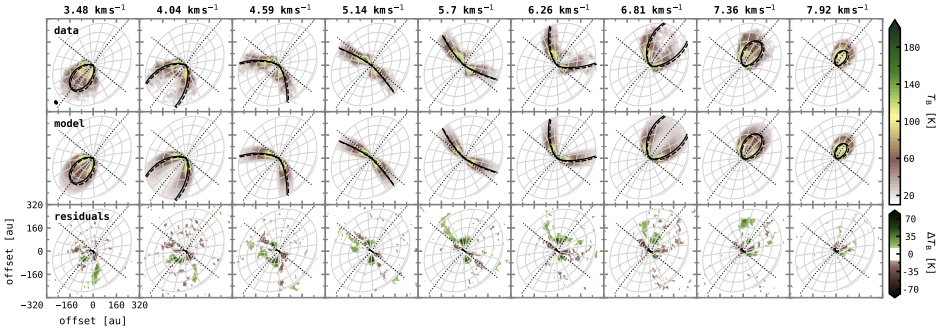


**Figure 5.C.1:** Same as in Fig. 5.5 but for $^{12}$CO 7-6.

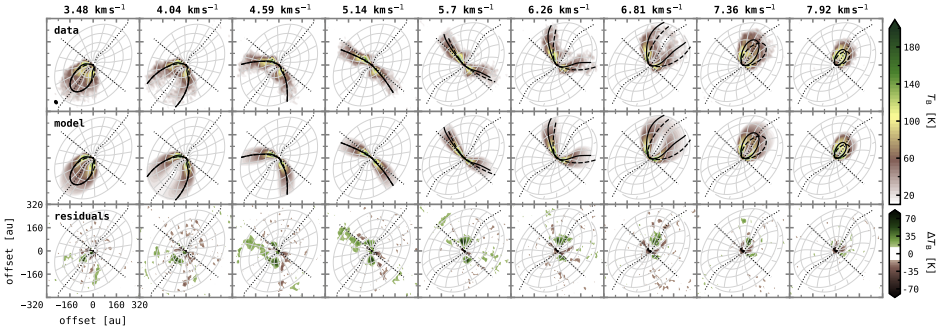


**Figure 5.C.2:** Same as in Fig. 5.5 but for $^{12}$CO 7-6 and the blue- and redshifted sides being modelled separately.

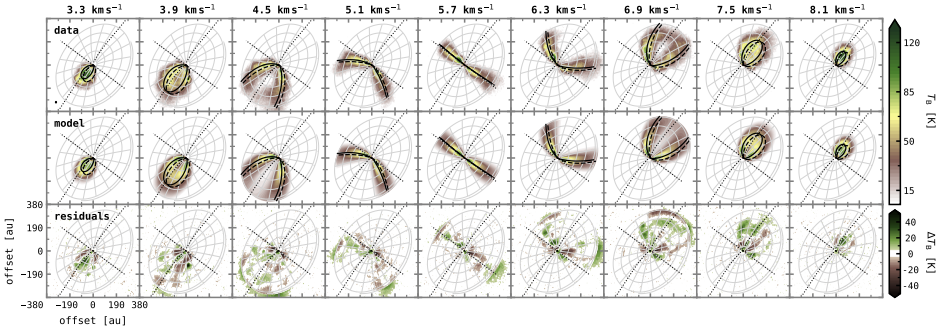


**Figure 5.C.3:** Same as in Fig. 5.5 but for $^{12}$CO 3-2.

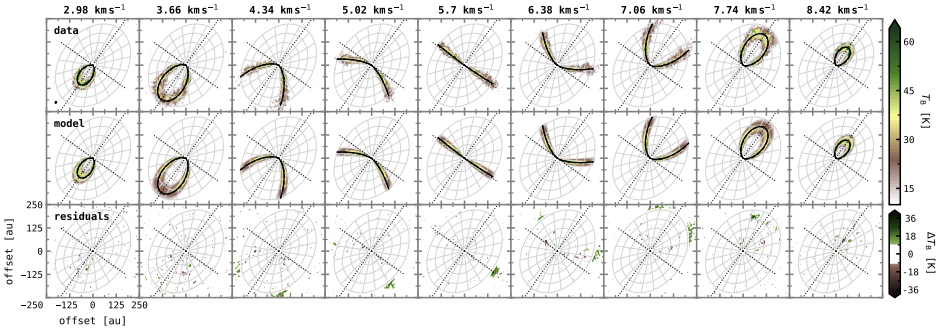


**Figure 5.C.4:** Same as in Fig. 5.5 but for $^{13}$CO 2-1.

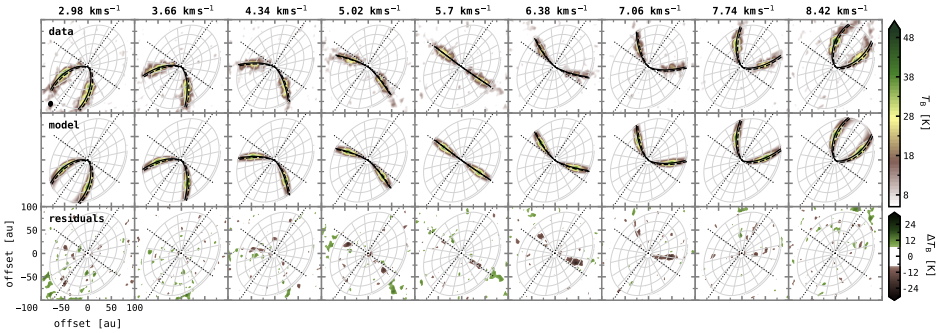


**Figure 5.C.5:** Same as in Fig. 5.5 but for C$^{18}$O 2-1.

## 5.D Logarithmic spirals

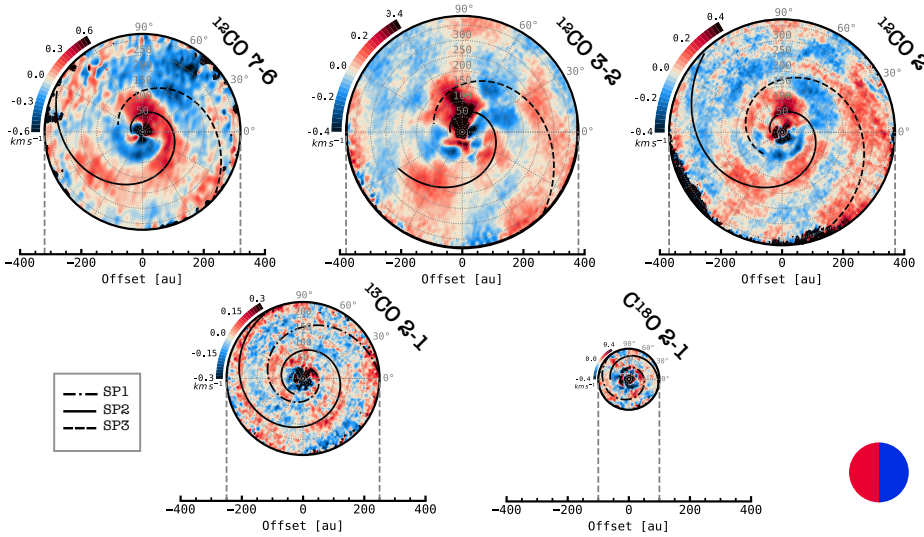


**Figure 5.D.1:** Same as in Fig. 5.7 but with overlaid logarithmic spirals.

## 5.E Peak intensity and line width residuals

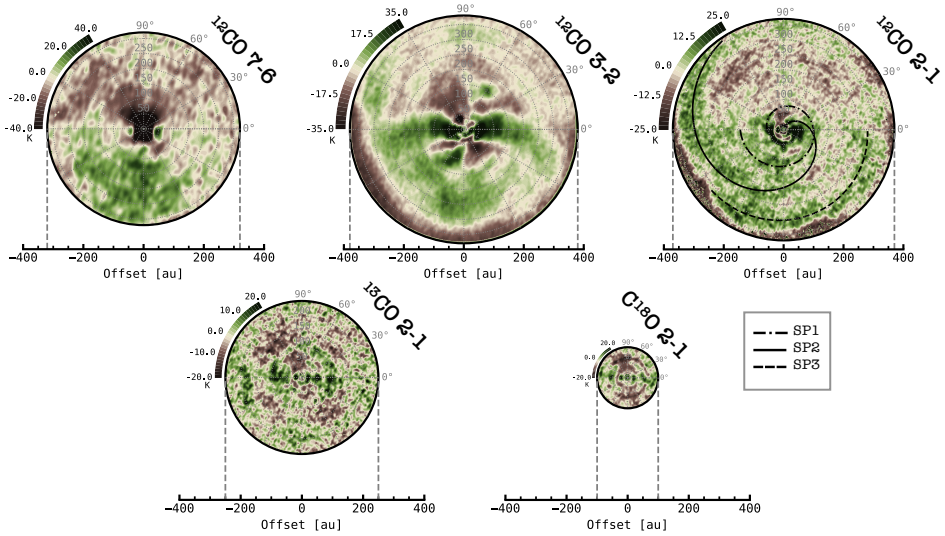


**Figure 5.E.1:** Peak intensity residuals, shown for the five lines studied in this work.

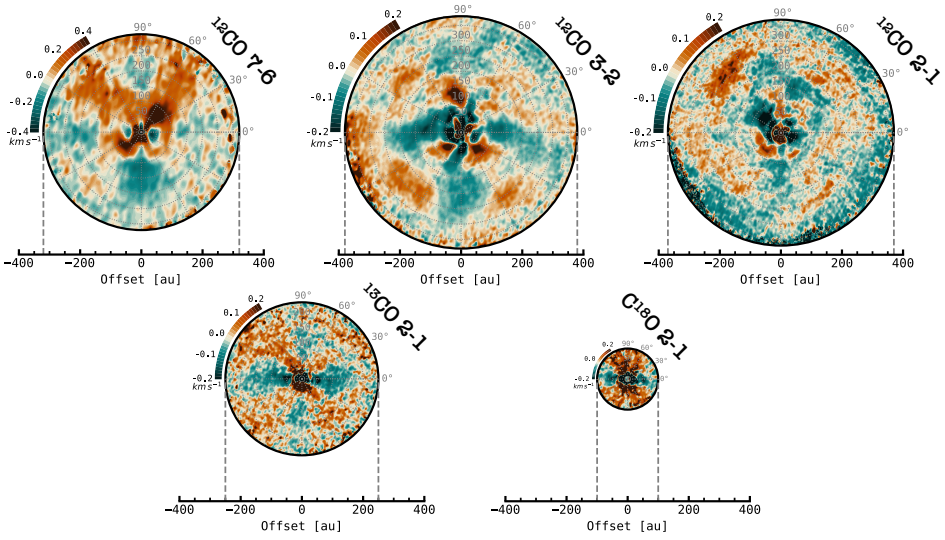


**Figure 5.E.2:** Line width residuals, shown for the five lines studied in this work.